Bulletin of Engineering Geology and the Environment (2024) 83:286
https://doi.org/10.1007/s10064-024-03779-7

ORIGINAL PAPER

Deciphering of karst geomorphology and sinkhole (doline) structures using multiple geophysical and geological methods (Trabzon, NE Türkiye)

Hilal Alemdağ[1] · Fatih Köroğlu[2,3] · Zeynep Öğretmen Aydın[1] · Aysel Şeren[1] · Ali Erden Babacan[1] · Arzu Fırat Ersoy[4]

Received: 10 December 2023 / Accepted: 9 June 2024
© The Author(s) 2024

Abstract

To date, in Türkiye only a limited number and volume of combined geophysical and geological studies about karst have been performed. In this study, karstification and geomorphological features were examined with geophysical and geological methods together and initial results were obtained for Türkiye. Although the geology of the limestone forming the Şahinkaya Member, which contains Çayırbağı, Çalköy, and Çal Cave, near the Düzköy district of Trabzon/Türkiye province was studied by many researchers to date, there is no geophysical study to determine the internal structural features, groundwater, dolines, and karstic voids. The aim of this study was to identify karst formations and their structural extensions in Şahinkaya Member with geophysical methods. Therefore, three different study locations with a total surface area of approximately 3.2 km^2 were examined with electrical resistivity tomography, self-potential, seismic refraction tomography, multichannel analysis of surface waves, and ground penetrating radar. These geophysical applications in limestone helped to identify karst cavities, water-saturated zones and dolines. Finally, the order of priority and efficiency of the five applied geophysical methods was compared, and the stages of the applications were outlined. In addition, the origin of karstification in the area investigated in this study was supported by petrographic, petrophysical and rock mechanic data.

Keywords Cave · Geophysical · Hydrogeological · Karst · Sinkhole (doline) · Şahinkaya Member

Introduction

In Eastern Sakarya Zone (NE Türkiye), Upper Cretaceous-Paleogene sedimentary cover (calciclastic, pelagic, hemipelagic, and neritic successions) was deposited after a volcanic arc sequence (Korkmaz 1993; İnan et al. 1999; Hippolyte et al. 2015; Köroğlu 2018; Köroğlu and Kandemir 2019b; Consorti and Köroğlu 2019; Consorti et al. 2020). Detailed studies about the biostratigraphy and sedimentology of the Maastrichtian-Paleocene shallow water

✉ Hilal Alemdağ
hilalalemdag@ktu.edu.tr

Fatih Köroğlu
fkoroglu1985@gmail.com

Zeynep Öğretmen Aydın
zogretmen61@gmail.com

Aysel Şeren
seren@ktu.edu.tr

Ali Erden Babacan
a.babacan@ktu.edu.tr

Arzu Fırat Ersoy
firat@ktu.edu.tr

[1] Faculty of Engineering, Department of Geophysical Engineering, Karadeniz Technical University, Trabzon 61080, Türkiye

[2] Faculty of Engineering, Department of Geological Engineering, Ankara University, Ankara 06100, Türkiye

[3] Tekfen Engineering, Tekfen Tower No: 209/1, Şişli/İstanbul 34394, Türkiye

[4] Faculty of Engineering, Department of Geological Engineering, Karadeniz Technical University, Trabzon, Türkiye

Published online: 25 June 2024

sequences overlying arc magmatism were carried out in the Eastern Sakarya Zone (Korkmaz 1993; İnan et al. 1999; Köroğlu 2018; Köroğlu and Kandemir 2019b; Consorti and Köroğlu 2019; Consorti et al. 2020).

In this study, the studied karst terrains are located between Çayırbağı and Çalköy (Düzköy, Trabzon) in the Black Sea (NE Türkiye). There are ~100 m thick neritic (shallow water) limestones dated to Upper Cretaceous-Paleogene age, known as the Şahinkaya Member (Köroğlu 2018; Köroğlu and Kandemir 2019b; Consorti and Köroğlu 2019; Consorti et al. 2020) in the region. The regional geology, stratigraphy (bio- and litho-) and partial hydrogeological/geophysical properties of the Tonya Formation and Şahinkaya Member were examined by Ofluoğlu (1993), Korkmaz (1993), Ayaz (1995), İnan et al. (1999), Hippolyte et al. (2015), Köroğlu (2018), Türk-Öz and Özyurt (2018), Köroğlu and Kandemir (2019a, b), Consorti and Köroğlu (2019), Consorti et al. (2020), Alemdağ et al. (2022, 2023). Korkmaz (1993) emphasised that the Şahinkaya Member consists of massive, locally thick-bedded, rudist limestones, and stated that the base of the member is reddish coloured and sandy limestones. Ofluoğlu (1993) indicated that there are dolines (with diameters ranging between ~4 and 55 m) and karstic cavities that developed in the Şahinkaya Member as a result of karstification. Ofluoğlu (1993) also stated that Çal Cave formed due to karstification.

Sinkholes (dolines), which vary in diameter and depth from a few meters to hundreds of meters, are the most common features in karst regions (Veress 2016; Öztürk 2018). They are open/closed depressions forming as a result of surface and groundwater dissolving mainly sedimentary or carbonate rocks. Dolines, which are proposed to be possible leakage routes for surface waters in hydrogeology (Valois et al. 2011), are split up in six classes according to their formation type. These are solution, collapse, caprock, dropout, suffusion and buried dolines (Doğan 2004; Waltham and Fookes 2005; Williams and Ziegler 2014; Veress 2016; Öztürk 2018; De Waele 2017). The formation process, host rock type, formation speed, typical maximum size, engineering hazard and other names for these doline classes are presented (Fig. 1).

Caves are natural underground voids, usually formed by the weathering of rocks. These structures, which can take millions of years to form, develop as a result of various factors such as tectonism, atmospheric effects, erosion by water, chemical processes, dissolution and microorganism activities (Balkaya et al. 2012). There are various cave classification schemes in the literature (Culver and White 2005; Klimchouk et al. 2006; Ford and Williams 2007; Oberender and Plan 2013, 2018; Bella and Gaal 2013; Mylroie 2019).Solution caves, which constitute most of the world's caves, occur in carbonate and sulphate rocks. These rocks are dissolved by natural acid in groundwater seeping from bedding planes, faults, joints, and irregular passages, which forms large cavities and eventually solution caves (Davies and Morgan 1987).

The subsurface heterogeneities that characterise karsts create a challenge for engineering and environmental studies. In such cases, integrated geophysical applications could offer a better way to look into the karst systems (Ford and Williams 2007; Putiska et al. 2014; Hussain et al. 2020). Geophysical investigations (e.g., electrical resistivity tomography (ERT), seismic refraction/reflection (SRT), ground penetrating radar (GPR), self-potential (SP), microgravity) have been used to detect the presence of sinkholes, caves and similar karstic structures without harming the investigated medium, especially in karst environments (Greenfield 1979; Valois 2010; Chalikakis 2011; Drahor 2019; Farfour et al. 2022; details in materials and methods).

This study provides new information about the internal structural properties of limestones (dolines, karstic voids, caves, etc.) using integrated geophysical methods for the first time in the Şahinkaya Member. In this context, geophysical data were acquired using ERT, SP, SRT, MASW, and GPR methods from three different areas in Şahinkaya Member. Based on the obtained data, dolines and their extensions, karstic voids and water-saturated areas within the study area were revealed. In addition, ranking of the priority and effective use of the five geophysical methods was performed and comparison of the results was made based on all geophysical data obtained from karst areas.

Geological Framework and Study Area

The areas investigated in the study are located in the Şahinkaya Member, which outcrops between Çayırbağı and Çalköy, and in the vicinity of Çal Cave in the Düzköy district of Trabzon/Türkiye (Fig. 2a–c). The reason for choosing this region is the presence of karstic cavities, sinkholes (dolines) (Fig. 3a-d), and Çal Cave containing an underground river (Fig. 3e-h).

The geology of the study area has been investigated by many researchers (Bulguroğlu 1991; Ofluoğlu 1993; Korkmaz 1993; Köroğlu 2018; Köroğlu and Kandemir 2019b; Consorti and Köroğlu 2019) to date. Based on these studies, the general geological information of the region is as follows: the Şahinkaya Member was first introduced as the Şahinkaya Formation by Bulguroğlu (1991) in a master's thesis entitled "*Geological Investigation of the Düzköy-Çayırbağı (Trabzon) Region*" and later named the Şahinkaya Member in the study entitled *"Stratigraphy of the Tonya-Düzköy (SW Trabzon), area"* by Korkmaz (1993). According to Korkmaz (1993), the Tonya Formation was deposited

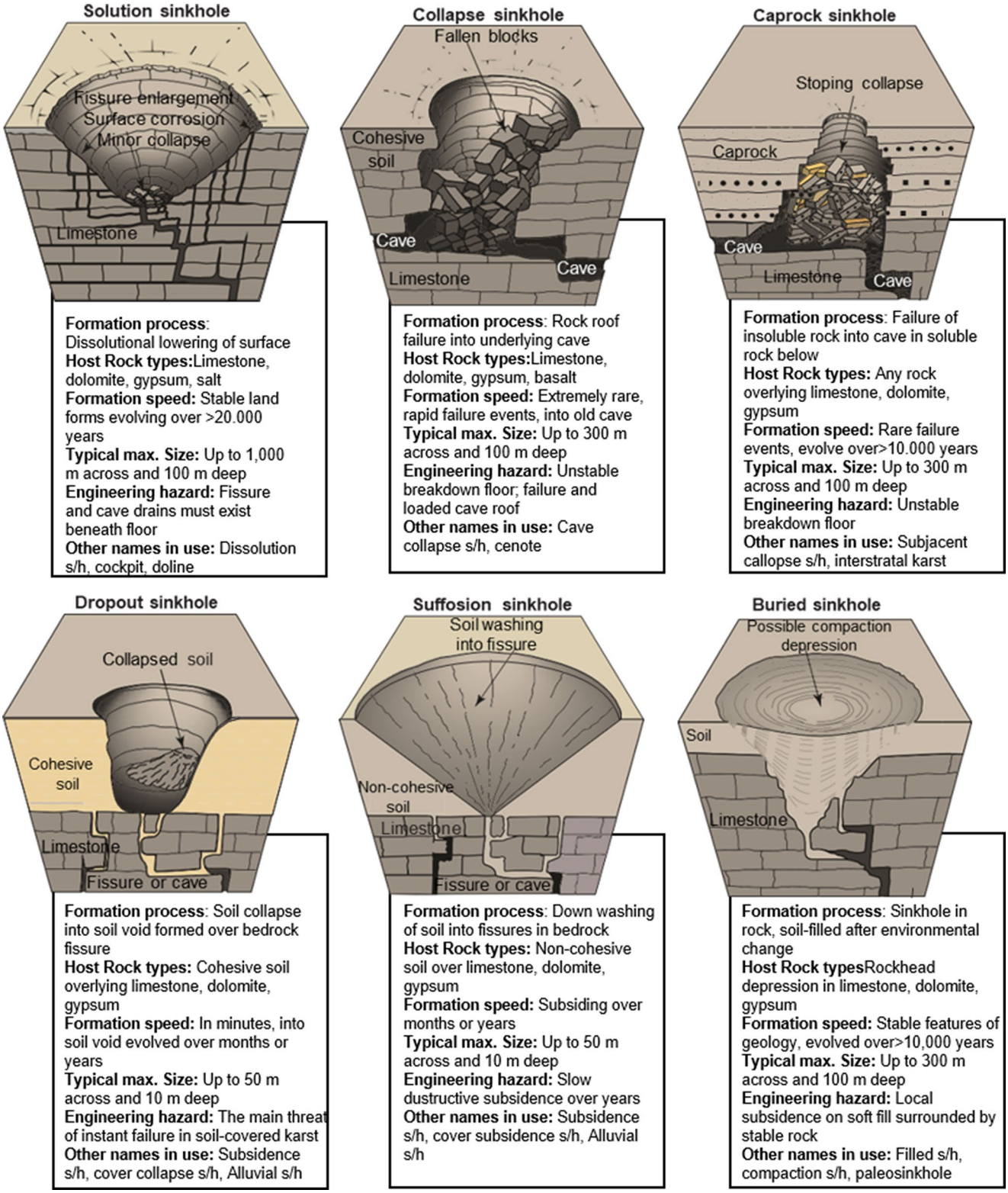


Fig. 1 Dolines (sinkholes) types (modified from Watham et al. 2005; McCraw and Land 2016; Öztürk 2018)

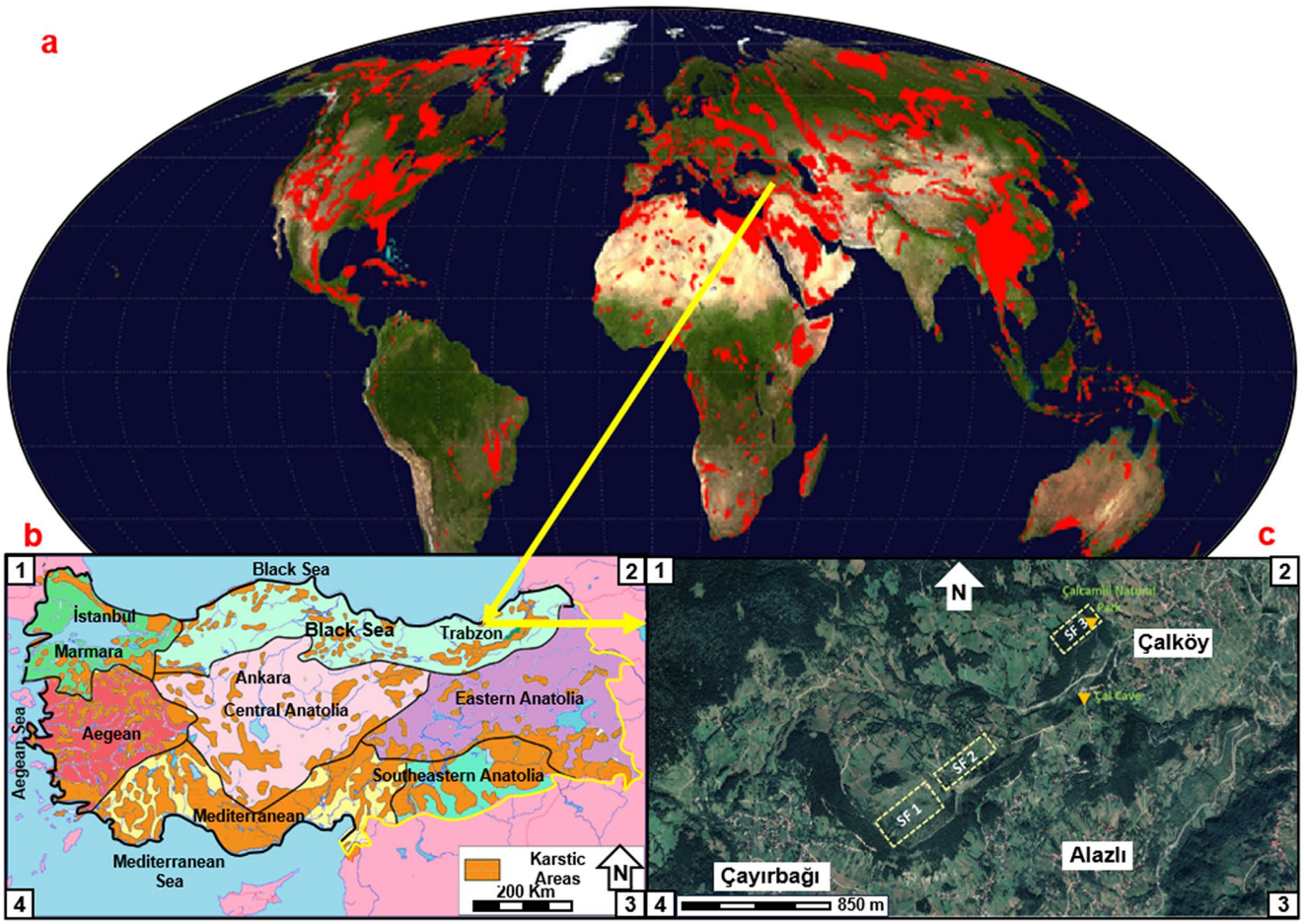


Fig. 2 Location map of the study field, (**a**) World Sinkhole Map (https://foundationtechs.com/world-and-usa-sinkhole-map/), (**b**) Karstic regions of Türkiye. (modified from Nazik and Poyraz 2017) (coordinate of b: 1 = 34°23'25.9"N, 37°58'44.10"E; 2 = 37°47'29.13"N, 36°39'35.67"E; 3 = 34°40'03.40"N, 44°50'22.88"E; 4 = 34°07'34.34"N, 26°10'51.47"E), (**c**) The study fields (coordinate of c: 1 = 40°52'16.52"N, 39°20'25.63"E; 2 = 40°52'43.90"N, 39°24'05.12"E; 3 = 40°51'16.52"N, 39°24'23.68"E; 4 = 40°50'48.69"N, 39°20'39.50"E)

in a pelagic and neritic environment based on lithological, palaeontological, and sedimentological features. However, the reef limestones (limestone containing the remains of reef-forming organisms such as coral and sponge etc.) that comprise the Şahinkaya Member formed due to shallow environment conditions in the central part of the study area. The Şahinkaya Member consists of massive, occasionally thick-bedded, rudist-bearing limestone, and red-coloured limestone and sandy limestone are present at basal levels (Bulguroğlu 1991; Korkmaz 1993; Köroğlu 2018; Köroğlu and Kandemir 2019b; Consorti and Köroğlu 2019). The geological map of the Düzköy region including the areas investigated in this study is shown in Fig. 4b, while the satellite image of the study area is shown in Fig. 4a.

The master's thesis entitled "*Investigation of the Karstification in Çalköy-Alazlı (Düzköy, Trabzon) Region*" by Ofluoğlu (1993) identified karstification occurring in the Çalköy-Alazlı region, the characteristics of structures formed as a result of karstification, and causes of karstification. Additionally, the general geological characteristics of the region were revealed. Ofluoğlu (1993), Törk et al. (2013), Köroğlu (2018), Köroğlu and Kandemir (2019a, b) stated that dolines with distinct dimensions, karstic voids and Çal Cave in the Şahinkaya Member formed due to karstification. Köroğlu (2018) conducted a study to reveal the distribution, thickness, rock type, sedimentary structure-texture relationships, micro characteristics, and fossil content of the neritic carbonates found in the region. Köroğlu (2018) took three measured stratigraphic sections to reflect the unit in the region of this study. The average thickness of the Şahinkaya Member was determined to be ~100 m (Köroğlu 2018), and it consists of thick-bedded, sandy, lithoclastic and bioclastic components, with red-coloured limestone and sandy limestones at some basal levels of the lithology (Korkmaz 1993; İnan et al. 1999; Köroğlu 2018; Köroğlu and Kandemir 2019b; Consorti and Köroğlu 2019; Consorti et al. 2020). In the Çayırbağı-Çalköy region, where measured stratigraphic sections were made, the unit mostly consists of fossil (rudist

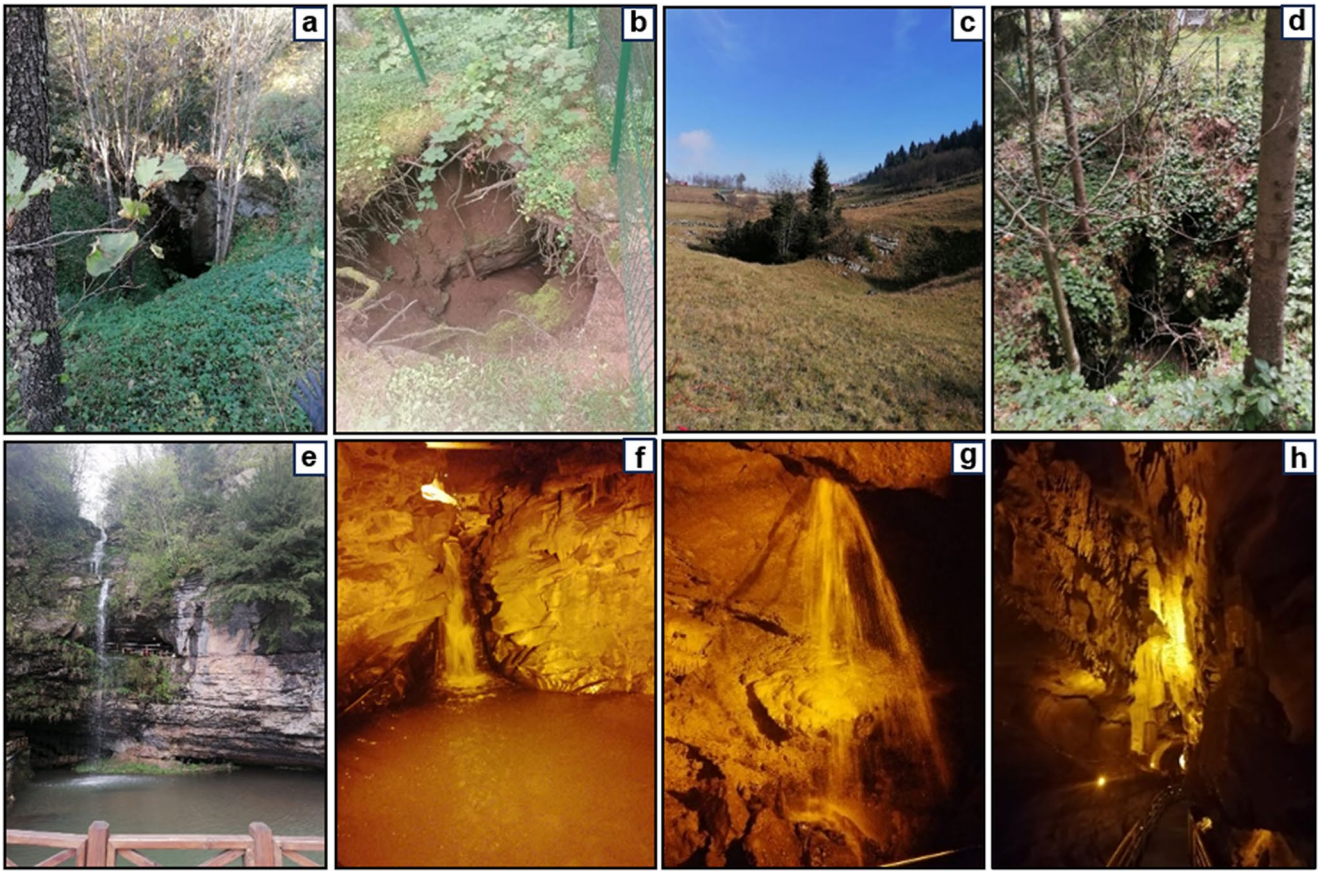


Fig. 3 Dolines and Çal cave around the study fields, (**a-d**) View of dolines in Çal Camili Natural Park and Şahinkaya Mezra, (**e**) The entrance to the Çal Cave, (**f**) The underground river flowing through the Çal Cave and the accumulation pool, (**g**) Water flowing from the siphon entrance of the Çal Cave, (**h**) The stalagmites-stalactites inside the Çal Cave

fragments) limestone that is massive or thick-layered, varying in colour from yellow to grey, and is occasionally clayey, sandy, dolomitic, and brecciated (Korkmaz 1993; İnan et al. 1999; Köroğlu 2018; Kandemir and Köroğlu 2019b; Consorti and Köroğlu 2019; Consorti et al. 2020). Karstic caves developed in typically steep hills formed by limestone that is highly fractured, soluble, and contains rudist shells (Ofluoğlu 1993; Korkmaz 1993; Özer et al. 2009; Törk et al. 2013; Köroğlu and Kandemir 2019a, b).

Materials and Methods

There are many geophysical (e.g., ERT, SP, GPR, SRT and MASW) studies in the literature about identifying the underground location, extension and spread of karstic formations such as dolines, karstic voids and caves.

Study Field 1 (SF1) is located at '*Kayaüstü Mezra'* (in Turkish) with an area of ~300 m x 400 m (Fig. 5a). SF1 was chosen for study because large-diameter dolines (Fig. 5b) and karstic voids were observed on the surface (Fig. 5c). Geophysical measurement profiles were selected to run perpendicular to the centre and around this doline considering its bowl shape. The distances between profiles are not equal and vary between ~15 and 35 m depending on surface conditions.

Study Field 2 (SF2), shown in Fig. 6a, is located between two hills. This area has very wet ground as it holds rainwater draining from the hills. In addition, dolines (Fig. 6b) and karstic voids (Fig. 6c) observed on the surface are also seen within this area. The reason for investigation of SF2 is that it was thought that one of the branches of Çal Cave passes through this area. A 600 m-long profile with NE-SW orientation was determined to vertically cut the cave branch. The data acquired in this area were limited to a single profile due to unsuitable field conditions.

Study Field 3 (SF3) is an area of ~200 m x 400 m (Fig. 7a). This area includes a forested area covered with pine trees. There are also dolines in SF3 with ~4–10 m diameter known to extend to very great depth (Fig. 7b, c).

Integrated geophysical methods (ERT, SP, SRT, MASW and GPR) were used to acquire data in these study fields. The internal structural features (caves, dolines, karstic

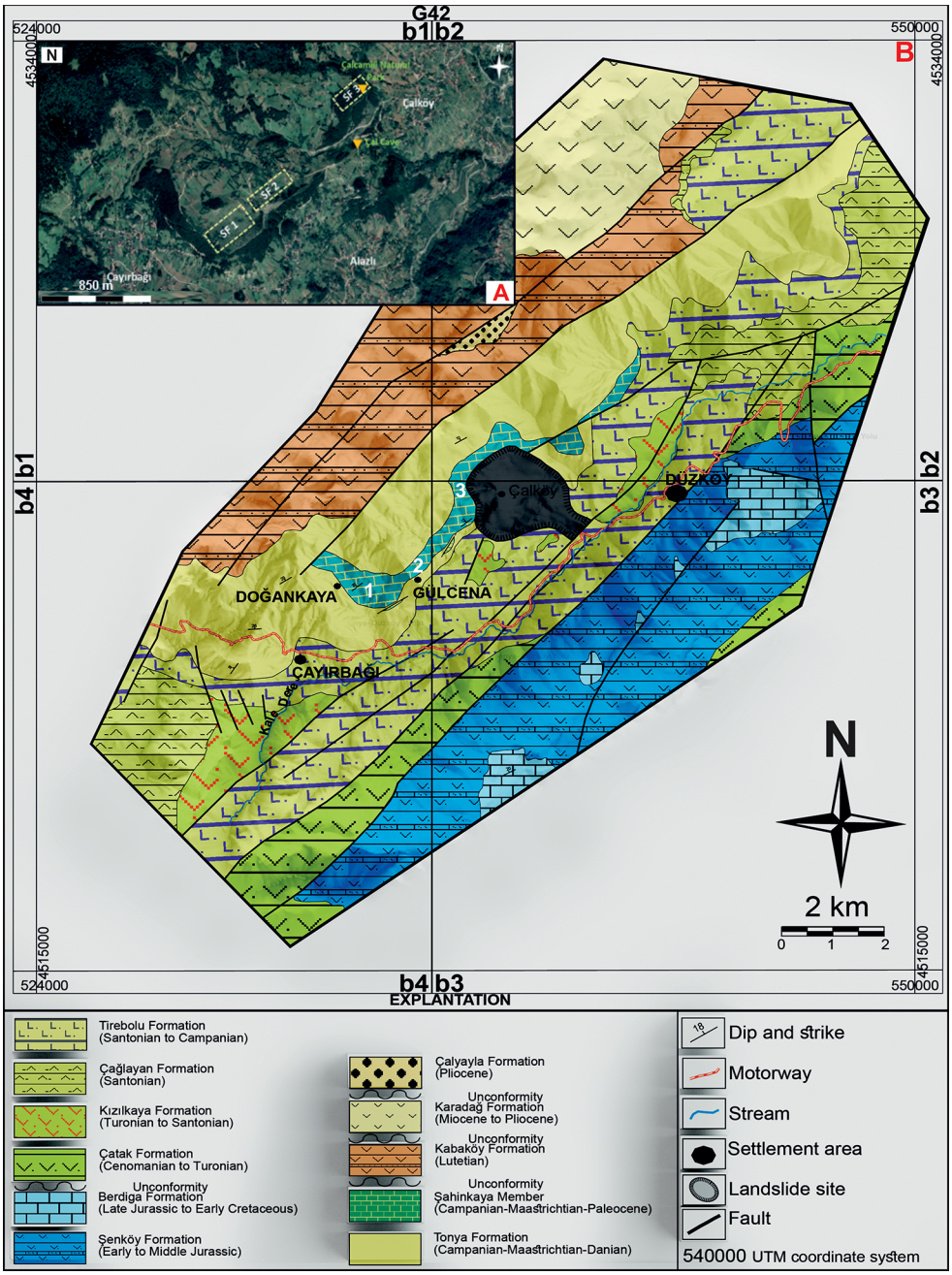


Fig. 4 (**a**) The study fields, (**b**) Geological map of Düzköy region where the study fields are located (modified from Köroğlu 2018; Köroğlu and Kandemir 2019b)

voids, etc.) of the limestone dominant in the study areas were revealed by evaluating the acquired data.

Electrical Resistivity Tomography

The ERT method is based on the principle that different types of subsurface materials have different electrical resistivity values. This method involves placing a set of electrodes on the ground surface. Then, an electrical current is passed through the material, and the resulting voltage differences are measured by the electrodes (Verdet et al. 2020). Thus, the apparent resistivity of the investigated medium is calculated, and the actual subsurface model is obtained by applying inverse and forward modelling to these values. This method is one of the most widely used geophysical methods in researching groundwaters (Kwon et al. 2005; Nyquist et al. 2008; Balakrishna et al. 2014; Kaufmann and Deceuster 2014; Xu et al. 2015; Khaldaoui et al. 2020; Hussain et al. 2020; Gelişli and Babacan 2021) and karstic structures such as sinkholes (dolines) (Zhou et al. 2000; Kaufmann and Romanov 2009; Valois et al. 2010; Abdallatif et al. 2015; Billi et al. 2016; Cueto et al. 2018; Drahor 2019; Fatma et al. 2020; Tao et al. 2022;), caves (McGrath et al. 2002; El-Qady et al. 2005; Andrej et al. 2012; Park et

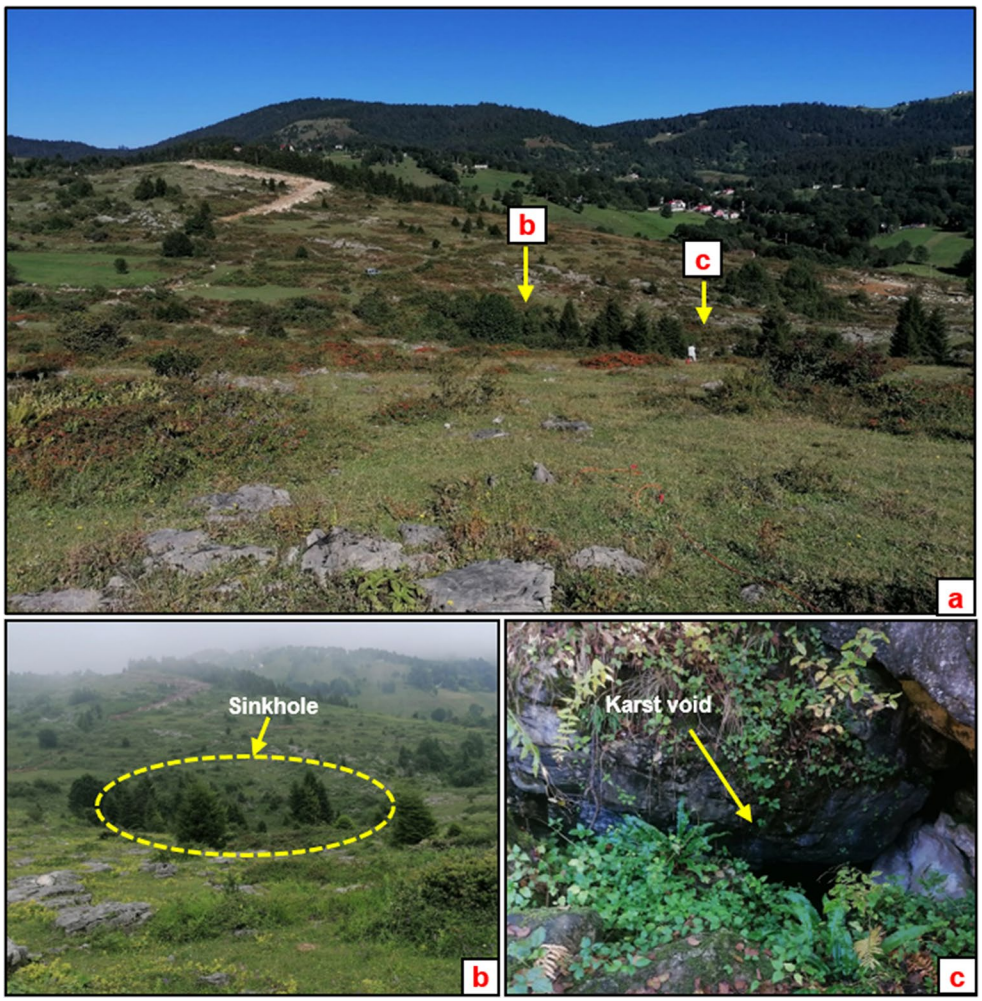


Fig. 5 Landforms of SF1, (**a**) Surface from which measurements were acquired, (**b**) Landforms view of the sinkhole in SF1, (**c**) Karstic voids found in SF1.

al. 2014; Abdallatif et al. 2015; Su et al. 2017; Sarıbudak and Hauwert 2017), soil and bedrock interface (Chalikakis et al. 2011; Bermejo et al. 2017; Cheng et al. 2019).

ERT data were obtained on the profiles determined in SF1 (ERT1_P1-ERT1_P7 with NW-SE orientation and ERT1_P8-ERT1_P10 with NE-SW orientation), SF2 (ERT2_P1 with NE-SW orientation) and SF3 (ERT3_P1-ERT3_P9 with NE-SW orientation and ERT3_P10-ERT3_P12 with NW-SE orientation).

The ABEM Terrameter LS 2 multi-electrode electrical resistivity instrument was used to collect ERT data. ERT data were acquired using the Wenner-Schlumberger array (Prins et al. 2019) to monitor the subsurface resistivity distribution in lateral and vertical orientations in the subsurface. ERT data acquisition parameters are given in Table 1.

The Res2dinv (Loke 2010) program was used to evaluate the 2-D ERT data. This program basically uses the least squares inversion technique (De Groot-Hedlin and Constable 1990). In the inversion scheme, since a sharp resistivity contrast between karst formations and the surrounding unit is expected, robust (L1 norm) model constraints were used that minimise the sum of the absolute values of changes in model resistivity (Loke 2010). The absolute (abs) errors were below 5% for all sections from three study areas. In addition, 3-D subsurface models (Figs. 10 and 11) were generated using the 2-D resistivity-depth sections obtained by inversion of raw apparent resistivity data and the locations of the measurement lines from which these sections were obtained.

Self-Potential

The SP method has a working principle based on measuring the voltage difference between any two points on the ground. Electric potential occurs naturally in the earth. The origin of self-potential generally arises from the charge separation in clay or other minerals, the presence of a semi-permeable interface that prevents the diffusion of ions from the pore space of rocks, or the natural flow of a conductive fluid (such as saline water) through rocks (Revil and Jardani 2013). Changes in self-potential can be observed both in the field and in wellbores, and these changes can be used

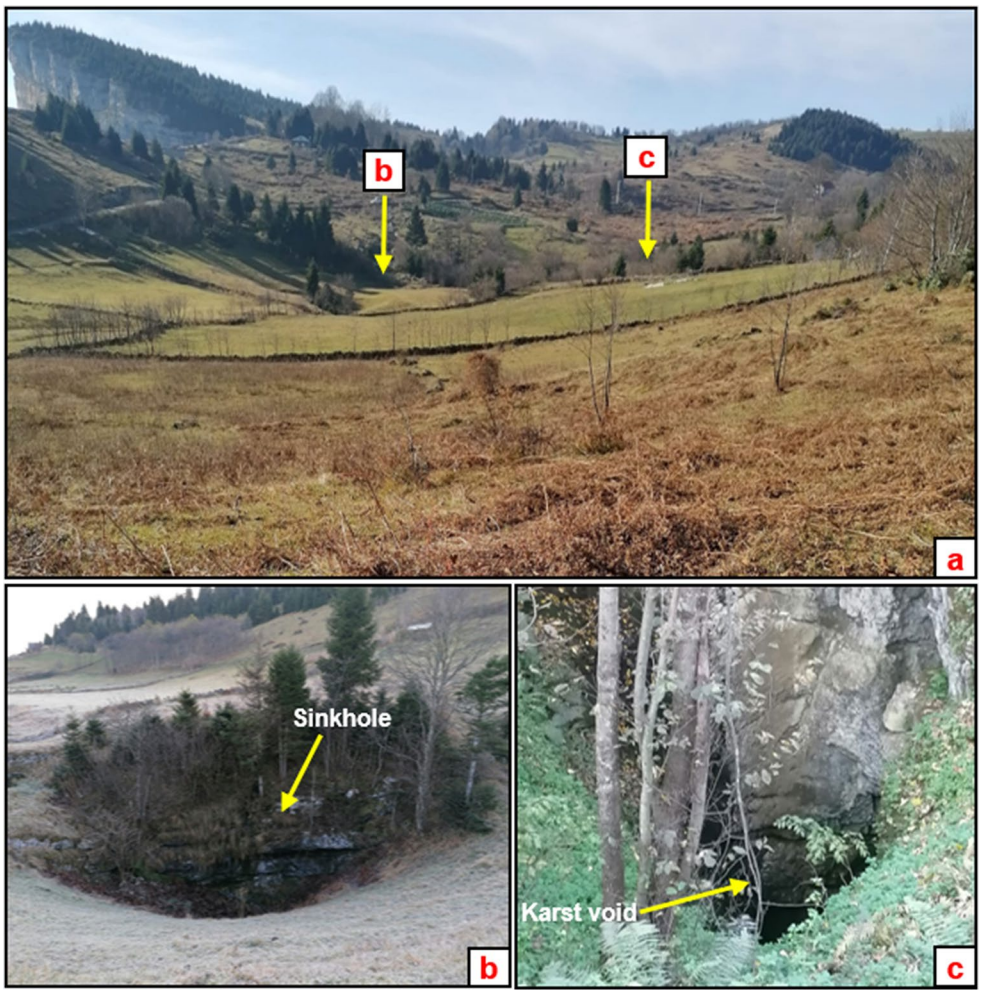


Fig. 6 Landforms of in SF2, (**a**) Surface from which measurements were acquired, (**b**) General view of the sinkhole in SF2, (**c**) View of karst voids found in SF2.

to detect variations in the ionic concentration of fluids in rock pores (Revil and Jardani 2013). This method is successfully used for the investigation of groundwater (Stevanovic and Dragisic 1998; Wanfang et al. 1999; Robert et al. 2011; Artugyan et al. 2015; Voytek et al. 2019), karst voids and sinkholes (dolines) (Lange 1999; Jardani et al. 2007; Cardarelli et al. 2013; Sarıbudak and Hawkins 2019).

The ERT sections obtained from SF1, SF2 and SF3 were evaluated and the regions showing anomalies in these sections were identified. SP measurements were taken in these anomalies regions. SP measurements were acquired on 7 profiles with NW-SE orientation and 3 profiles with NE-SW orientation in SF1; 1 profile with NE-SW orientation in SF2; and 9 profiles with NE-SW orientation and 3 profiles with NW-SE orientation in SF3. The length of the SP profiles varied between 115 and 270 m.

In the SP measurements, a multivoltmeter with high sensitivity and two non-polarised ceramic cup electrodes were used. To measure the natural potential difference during the measurement, one pot was fixed at the starting point and the other pot was moved at 5 m intervals. Before and after starting the measurement, the potential differences between the two pots and the times when these differences were measured were recorded. SP data may change gradually depending on external effects (climatic conditions and environmental effects) that vary over time. These changes may emerge as a temporal shift in the data. Therefore, drift correction was applied to SP data in order to eliminate this shift from the data. With this correction, the temporal drift is corrected assuming a shift between successive base station readings (Wanfang et al. 1999). The measured SP data were plotted as an SP graph and then 2-D SP maps were prepared from the SP graph. Interpretation of the data provided information about the subsurface fluid flow, and other geological features.

Seismic Refraction Tomography

The SRT method uses the principles of seismic wave propagation to determine the subsurface structure of the Earth. It is a non-invasive method that provides information about the velocity and depth of rock and soil layers, which can

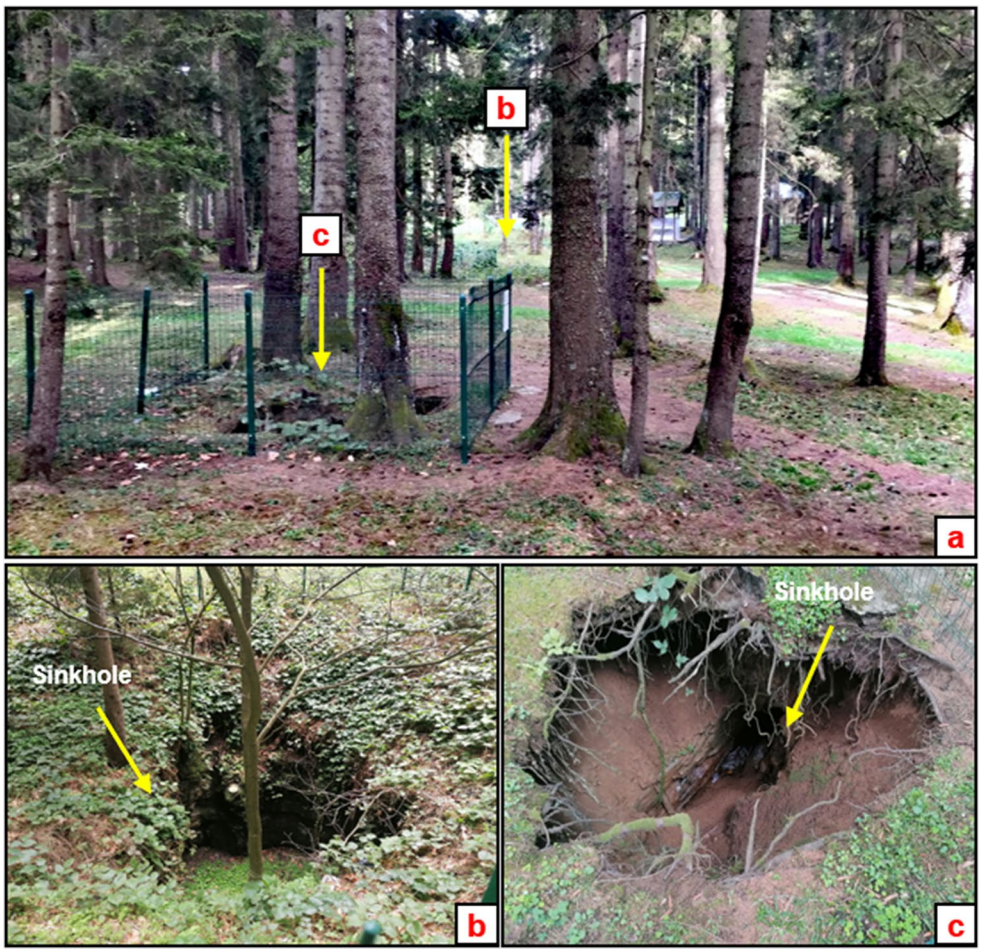


Fig. 7 Landforms from SF3, (**a**) Surface from which measurements were acquired, (**b-c**) Sinkholes observed from the surface within SF3.

Table 1 Measurement information of ERT data obtained from all study fields (SF1, SF2, and SF3) identified in Şahinkaya Member

Study Fields	Profile name/Orientation	Profile Length (m)	Electrode Spacing (m)	Electrode Number	Vertical Stack
SF1	ERT1_P1-P7/ NW-SE	300	7.5	41	3
	ERT1_P8-910/ NE-SW	400	5	61	3
SF2	ERT2_P1/ NE-SW	600	7.5	61	3
SF3	ERT3_P1-P9/ NE-SW	400	5	61	3
	ERT3_P10-P12/ NW-SE	200	5	41	3

be used to create a 2-D or 3-D model of the subsurface structure. The method works by recording the time it takes for seismic waves to travel through the subsurface and be refracted or reflected at boundaries between different layers of rock or soil. The distance-time (x-t) plot is obtained by picking the first arrival times of the seismic trace on the recorded data. The velocity and thickness of the subsurface layers are be determined by analysing the resulting x-t plot (Telford et al. 1991). This method is widely used to examine fault zones in karstic areas (Venkatanarayana and Rao 1989; Carpenter et al. 2003; Hiltunen and Cramer 2008; Cardarelli et al. 2010; Chalikakis 2011; Martinez-Moreno et al. 2014; Imposa et al. 2017; Gan et al. 2017; Cueto et al. 2018), groundwater potential, weathered layer thickness, possible cracked zones and underground geology (Young et al. 1998; Ugwu and Nwankwoala 2008; Sayed et al. 2012; Orojah and Agayina 2014; Cueto et al. 2018; Babacan et al. 2018).

SRT data were obtained for the profiles determined in SF1 (SRT1_P1-SRT1_P4 with NW-SE orientation and SRT1_P5-SRT1_P6 with NE-SW orientation), SF2 (SRT2_P1 with NE-SW orientation) and SF3 (SRT3_P1-SRT3_P10 with NE-SW orientation and SRT3_P11-SRT3_P15 with NW-SE orientation).

During data acquisition, a Pasi 24 channel seismic device and 24 geophones with 4.5 Hz were used. More details on the SRT application are given in Table 2.

SRT data obtained in this study were analysed using the SeisImager software, which is based on the nonlinear least squares method (Geometrics 2009). Initially, the first arrival times on the seismic traces recorded at each station were

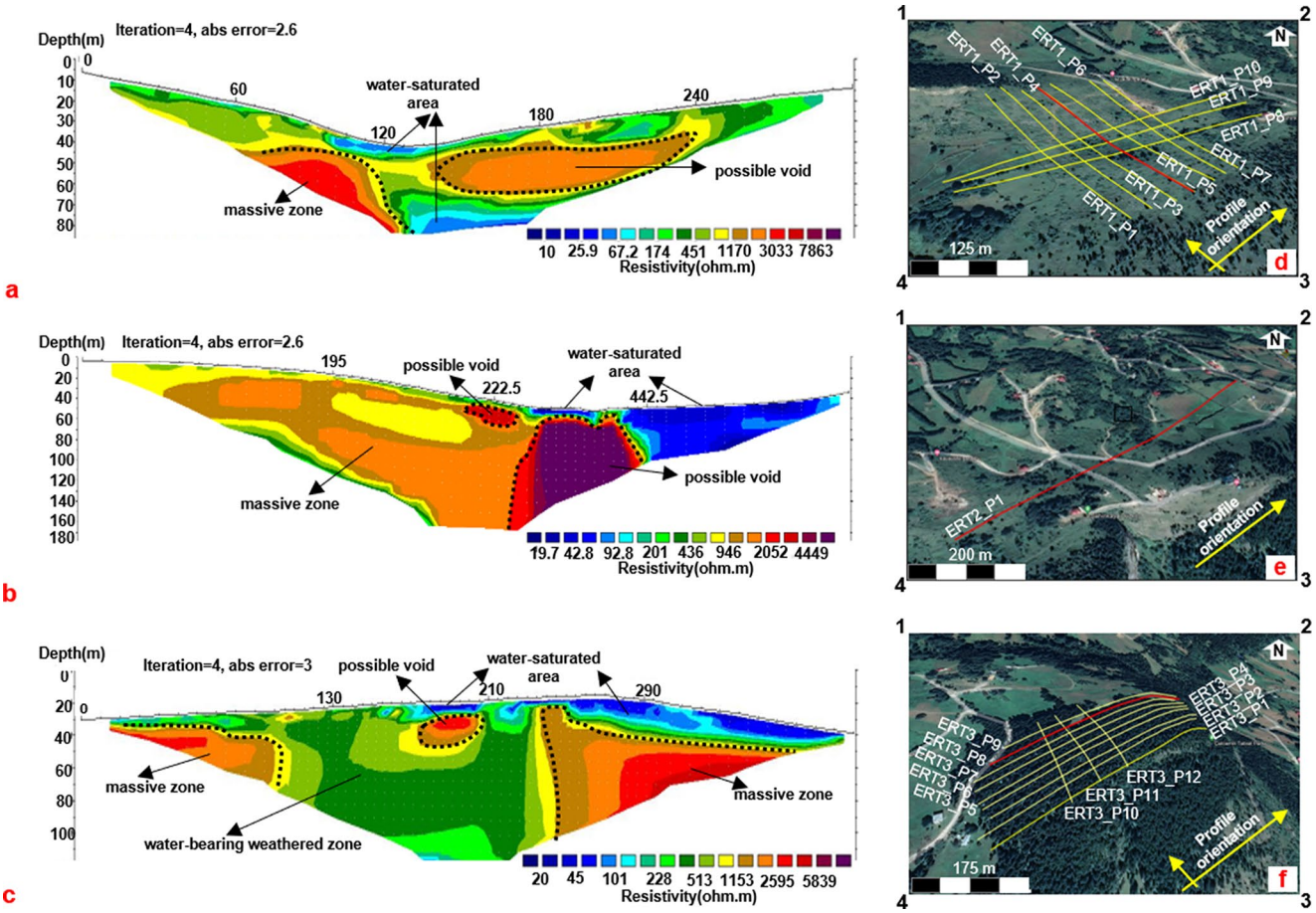


Fig. 8 ERT sections obtained from the study fields, (**a**) ERT1_4 section from SF1, (**b**) ERT2_1 section from SF2, (**c**) ERT3_8 section from SF3. Profiles (red lines) from which the graphs shown in a, b and c was acquired, are given (**d**) Application map of SF1 (coordinate of d: 1 = 40°51'38.36"N, 39°21'37.42"E; 2 = 40°51'39.70"N, 39°22'04.20"E; 3 = 40°51'20.67"N, 39°22'00.31"E; 4 = 40°51'21.73"N, 39°21'40.85"E), (**e**) Application map of SF2 (coordinate of e: 1 = 40°51'47.28"N, 39°21'44.10"E; 2 = 40°51'44.76"N, 39°22'17.43"E; 3 = 40°51'26.77"N, 39°22'11.74"E; 4 = 40°51'25.18"N, 39°21'48.70"E) and (**f**) Application map of SF3 (coordinate of f: 1 = 40°52'23.13"N, 39°22'26.72"E; 2 = 40°52'36.19"N, 39°23'06.80"E; 3 = 40°52'01.78"N, 39°22'53.17"E; 4 = 40°52'00.71"N, 39°22'34.59"E), respectively

picked to obtain x-t plots. The underground model generated as the initial model for tomographic inversion is used in the program. The minimum and maximum velocity values with the number of layer parameters are entered into the program by the user in order to create the initial model. Then, the program generates an underground model that increases in velocity with depth. Tomographic inversion uses the simultaneous iterative reconstruction technique (SIRT) (Gilbert 1972). This technique is one of the featured iterative reconstruction techniques (Lehmann 2007). The calculated curves obtained using ray tracing coincide with the observed curves. At this stage, if the compatibility is achieved with the expected error rate, the process is terminated. Thus, the subsurface structure and Vp velocity distribution are obtained.

Multichannel Analysis of Surface Waves

Multichannel analysis of surface waves (MASW) is a suitable tool for sinkhole exploration due to the ability to distinguish between different kinds of unconsolidated soil and bedrock using changes in shear-wave velocity (Odum 2007; Parker and Hawman 2011; Nwokebuihe et al. 2014; Obi 2016).

MASW measurements were taken for the first 56 m of the seismic refraction tomography profiles. The receiver spacing was set at a distance of 2 m and the source offset was determined as 10 m for all profiles.

MASW data were acquired for profiles determined in SF1 (MASW1_P1-MASW1_P4 with NW-SE orientation and MASW1_P5-MASW1_P6 with NE-SW orientation), SF2 (MASW2_P1 with NE-SW orientation) and SF3 (MASW3_P1- MASW3_P10 with NE-SW orientation and

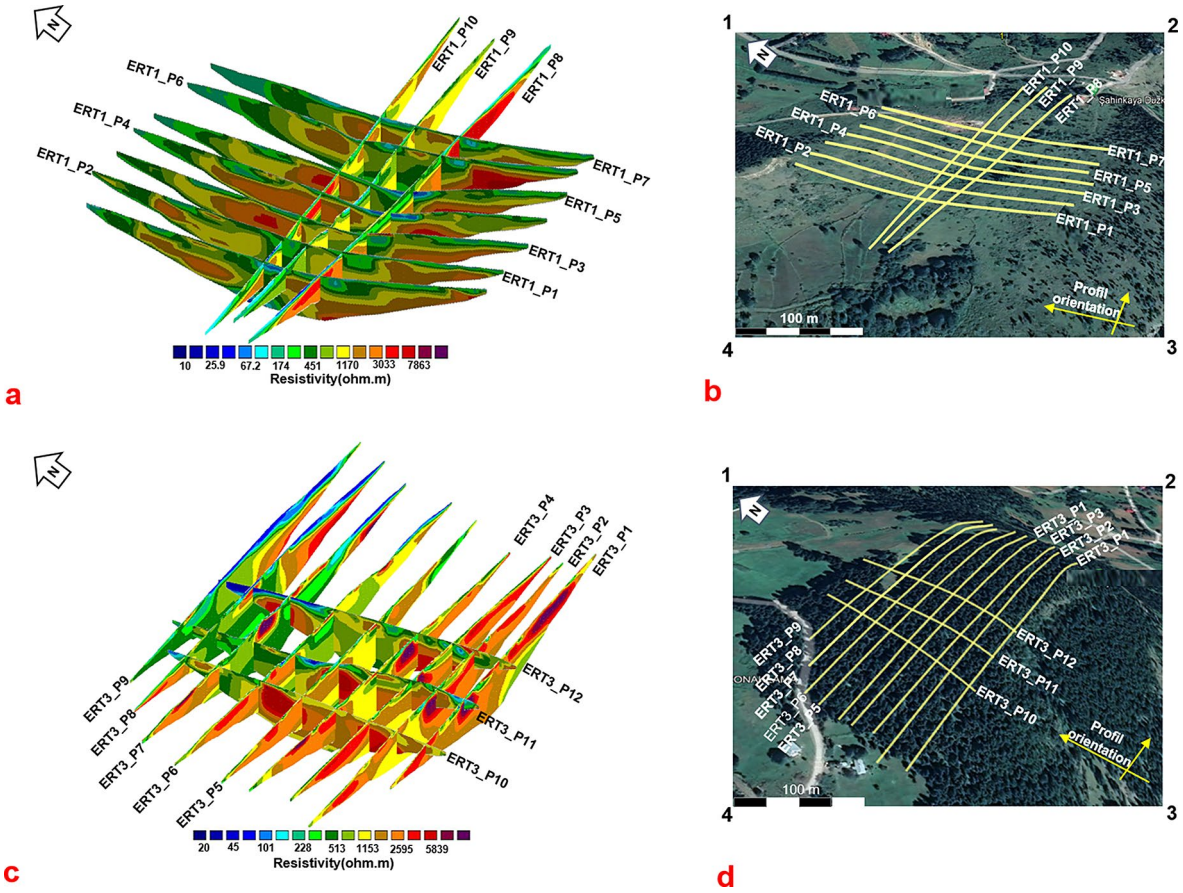


Fig. 9 A Fence diagrams of inverted ERT sections obtained from the SF1 and SF3, (**a**) A fence diagram from SF1, (**b**) Profiles from which the sections shown in A was acquired (coordinate of b: 1 = 40°51'42.76''N, 39°21'49.33''E; 2 = 40°51'32.69''N, 39°22'12.37''E; 3 = 40°51'16.74''N, 39°21'50.36''E; 4 = 40°51'22.84''N, 39°21'40.30''E), (**c**) 3-D fence diagram from SF3, (**d**) Profiles from which the sections shown in c was acquired (coordinate of d: 1 = 40°52'21.72''N, 39°22'39.22''E; 2 = 40°52'23.49''N, 39°23'05.04''E; 3 = 40°51'58.65''N, 39°22'46.18''E; 4 = 40°52'02.87''N, 39°22'33.12''E)

MASW3_P11- MASW3_P15 with NW-SE orientation). The same equipment used for the SRT method was used to collect the data. Information selected when collecting MASW data in the study fields are given in Table 3.

MASW data was also analysed using SeisImager software (Geometrics 2009), which utilises the weighted damped least-squares method, a commonly used deterministic approach. Several different methods such as phase-shift, f-k and Radon transform are used to obtain a dispersion curve (Yılmaz 1987; Park 1998; Luo et al. 2008). The most commonly used method is the phase-shift method. In this method, the surface wave records collected from the field are decomposed into separate frequency components using Fast Fourier Transform (FFT) (Park et al. 1998). Then, the amount of phase shift is determined to compensate for the time delay corresponding to a specific offset, and this is applied to each component for a specific phase velocity. All components are summed to create a combined amplitude corresponding to the velocity phase at that frequency (Eker 2009). Subsequently, an iterative solution is applied to the obtained dispersion curve. The initial models used during MASW solutions were determined by the software based on the characteristics of the dispersion curves. The depth and number of layers were specified by the user when creating the initial model. Finally, a one-dimensional Vs wave velocity depth model was obtained from this initial model using an inverse solution method based on nonlinear least squares.

Ground Penetrating Radar

The GPR method is used to determine the locations and characteristics of subsurface features, objects, and structures. It works by sending high-frequency electromagnetic waves into the ground using a transmitting antenna and receiving the reflected signals using a receiving antenna. As the electromagnetic waves travel through the ground, they interact with different subsurface materials and reflect back to the receiving antenna. The two-way travel time required for the waves to reflect back to the antenna is measured, and this information is used to calculate the depth and location

of subsurface objects by using the velocity of electromagnetic waves (Davis and Annan 1989). This method is also widely used for doline (Batayneh et al. 2002; Leucci 2006; Kruse et al. 2006; Delle Rose and Leucci 2010; Rodriguez et al. 2014; Pandey et al. 2019; Sevil et al. 2017; Lago et al. 2022; Hussain et al. 2020), cave (McMechan et al. 2002; Şeren et al. 2012; Martinez-Moreno et al. 2013, 2014; Lyskowski et al. 2014; Gosar and Ceru 2016; Ceru et al. 2018; Hussain et al. 2020) and shallow groundwater exploration (Nakashima et al. 2001; Gloaguen et al. 2001; Doolittle et al. 2006; Gomez-Ortiz et al. 2009; Idi and Kamarudin 2011; Mahmoudzadeh et al. 2012; Hengari et al. 2013; Dhakate et al. 2015; Kowalczyk et al. 2018).

GPR data were collected along selected profiles in suitable areas of the three study fields. These profiles were selected to be feasible under the field conditions due to rock outcrops and dense vegetation in some parts. In this context, GPR data were acquired on 17 profiles with NW-SE orientation and 2 profiles with NE-SW orientation in SF1; 1 profile with NE-SW orientation in SF2; and 39 profiles with NE-SW orientation and 10 profiles with NW-SE orientation in SF3. The data were obtained using the common offset data acquisition technique.

During data collection, an unshielded 100 MHz antenna from Mala company, and a Proex Control Unit were used. In addition, measurement information for GPR data is given in Table 4.

The Reflexw program (Sandmeier 2015) was used for processing GPR data. Basic data processing steps, including dewow, gain, and background removal, were applied to the GPR data to make 2-D data interpretable. However, advanced data processing steps such as bandpass filtering were applied at the user's discretion for data with poor image quality even after basic data processing steps. In addition, considering the study area was composed of limestones, an electromagnetic wave velocity of 0.12 m/ns for limestones was used for time-depth conversion (Robinson et al. 2013).

Review of Karst System Features

Karst Terrain of the Eastern Black Sea Region

The term 'Pontides' was first used by Hamilton (1842) for northern-east Anatolia and part of the Caucasus. The term covers part of the Alpine-Himalayan orogenic belt, which starts from Spain and crosses Anatolia along the Black Sea coast and reaches the Indian platform (Osswald 1912; Ketin 1966; Robinson et al. 1995; Okay and Şahintürk 1997; Nikishin et al. 2015a, b). Yılmaz et al. (1997) classified the Pontides in three categories as 'Eastern', 'Central' and 'Western'. The Eastern Black Sea region in Türkiye, which consists of a mountain chain ~600 km long E-W and ~200 km N-S (Özsayar et al. 1981; Okay and Şahintürk 1997; Köroğlu and Kandemir 2019b; Consorti and Köroğlu 2019), is called the 'Eastern Pontides' (Ketin 1966; Yılmaz et al. 1987; Okay and Şahintürk 1997). The region comprises a variety of pre-Carboniferous to Cenozoic igneous, sedimentary, and metamorphic rocks. The karst area in the Eastern Black Sea Mountains consists of Upper Cretaceous-Paleocene-Eocene clayey limestones located at lower levels than the Jurassic-Cretaceous limestones (Ofluoğlu 1993; Zaman et al. 2011; Nazik and Poyraz 2017). Splitting by streams, climatic changes and block uplift associated with Cenozoic sea level movements played an important role in the geomorphological development of these karst areas. In the upper levels of this karst area, there are various karst formations such as polje, uvala and dolines from the palaeokarstic period (Ofluoğlu 1993; Zeybek 2010; Nazik and Poyraz 2015, 2017). Cave development in this region is very limited since the rocks suitable for dissolution in the Eastern Black Sea Mountains karst region outcrop in limited areas (Nazik and Bayarı 2018). Some of these caves are (i) Karaca (Torul-Gümüşhane), (ii) Çımağıl (Merkez-Bayburt), (iii) Çal (Düzköy-Trabzon), (iv) Kuzalan Travertine (Dereli-Giresun), and (v) Yazkonağı (Ünye-Ordu) (Ofluoğlu 1993; Ersoy et al. 2006; Zaman et al. 2011; Uzun et al. 2015; Nazik and Bayarı 2018).

Implications

ERT sections obtained from SF1 have similar characteristics. When the ERT1-P4 section (this section is given as an example as it perpendicularly cuts the doline observed on the surface) in Fig. 8a is examined, information was obtained from a depth of ~60 m. It is remarkable that there is a low resistivity zone starting between 97.5 and 145 m along this profile length, narrowing gradually towards 30 m depth and expanding again as it goes deeper. There are high resistivity zones on the right and left sides of this low resistivity zone. The left zone (~3833 ohm.m) has higher resistivity values than the right zone (~1178 ohm.m). The zone on the right side could potentially be a void due to its narrowing shape. Air-filled cavities have higher resistivity value than solid rock (Chitea et al. 2019; Doyoro et al. 2021). Possible underground cavities may contain water and wet clay due to weathering and groundwater flows in the Şahinkaya Member, according to detailed geological information for the areas investigated in this study. Therefore, the reason why there is lower resistivity of the part interpreted as a 'possible void' in the ERT1_P4 section given in Fig. 8a compared to the zone called 'massive rock' may be because the cavity contains water or wet clay. In addition, there are zones of

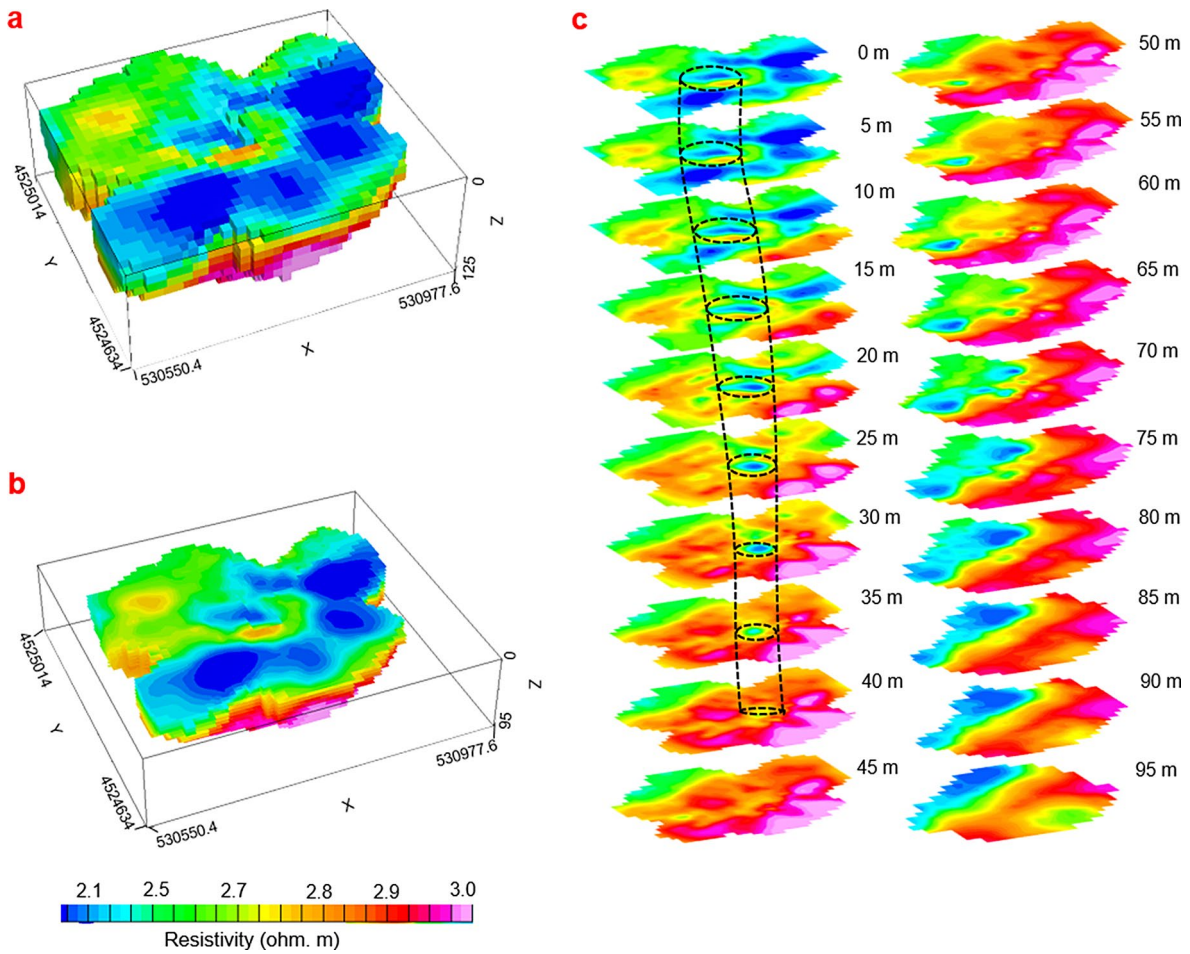


Fig. 10 3-D ERT images and level maps acquired from SF1, (**a**) 3-D ERT image acquired from SF1, (**b**) 3-D ERT image level maps displayed together, (**c**) 3-D ERT image level maps displayed every 5 m

low resistivity at depths of ~5 and 55 m from the surface from ~100–145 m of the axis length. Studies in the literature (Singh et al. 2019; Gelişli and Babacan 2021) indicate that these zones may be highly saturated with water.

In Fig. 8b, when the 600 m ERT2_P1 section obtained from SF2 is examined, a depth of ~120 m was imaged. Very high resistivity (~4449 ohm.m) was observed between 360 and 420 m, starting 9 m from the surface and continuing to a depth of 90 m in this section. In addition, very low resistivity (51.7 ohm.m) values were observed in the axis length range of 420–600 m of this section. Finally, a massive zone with resistivity values of ~1499 ohm.m was shown in the resistivity section.

When looking at the ERT3_P8 section from SF3, which is located in a forested area, information was obtained from a depth of ~80 m (Fig. 8c). A very thin cover layer thickness was observed on the surface throughout the section. This thickness was ~9 m. The same section had a 1153 ohm.m resistivity zone that widened as it goes deeper, starting from 75 to 267.5 m from the surface along the length axis. Areas with higher resistivity (2595 ohm.m) were observed on the right and left sides of this zone. In addition, the resistivity between 215 m and 400 m was quite low (~20 ohm.m). These regions are thought to be highly water-saturated.

ERT results are presented as fence diagrams, and underground models were created from the longest profiles with ERT data in SF1 and SF3 (Fig. 9a and c). Thus, an attempt was made to display the underground structure of these areas in detail. Fence diagrams constructed with inverted resistivity images along the profiles in SF1 and SF3 are shown in Fig. 9a and c, respectively. The low and high resistivity regions in these diagrams effectively revealed the underground karst features, such as water-saturated zones, karstic voids and massive zones laterally. The area of intersection of the ERT3_P7-P9 and ERT3_P10-12 sections on the fence diagram in Fig. 9c has low resistivity values. This area is considered to be a water-saturated area. In Fig. 9a, parts with low resistivity (<451 ohm.m) show these areas. The regions of closures (~2100 ohm.m resistivity) with lateral continuity in Fig. 9a were evaluated as possible voids, and regions with high resistivity to the south were interpreted as

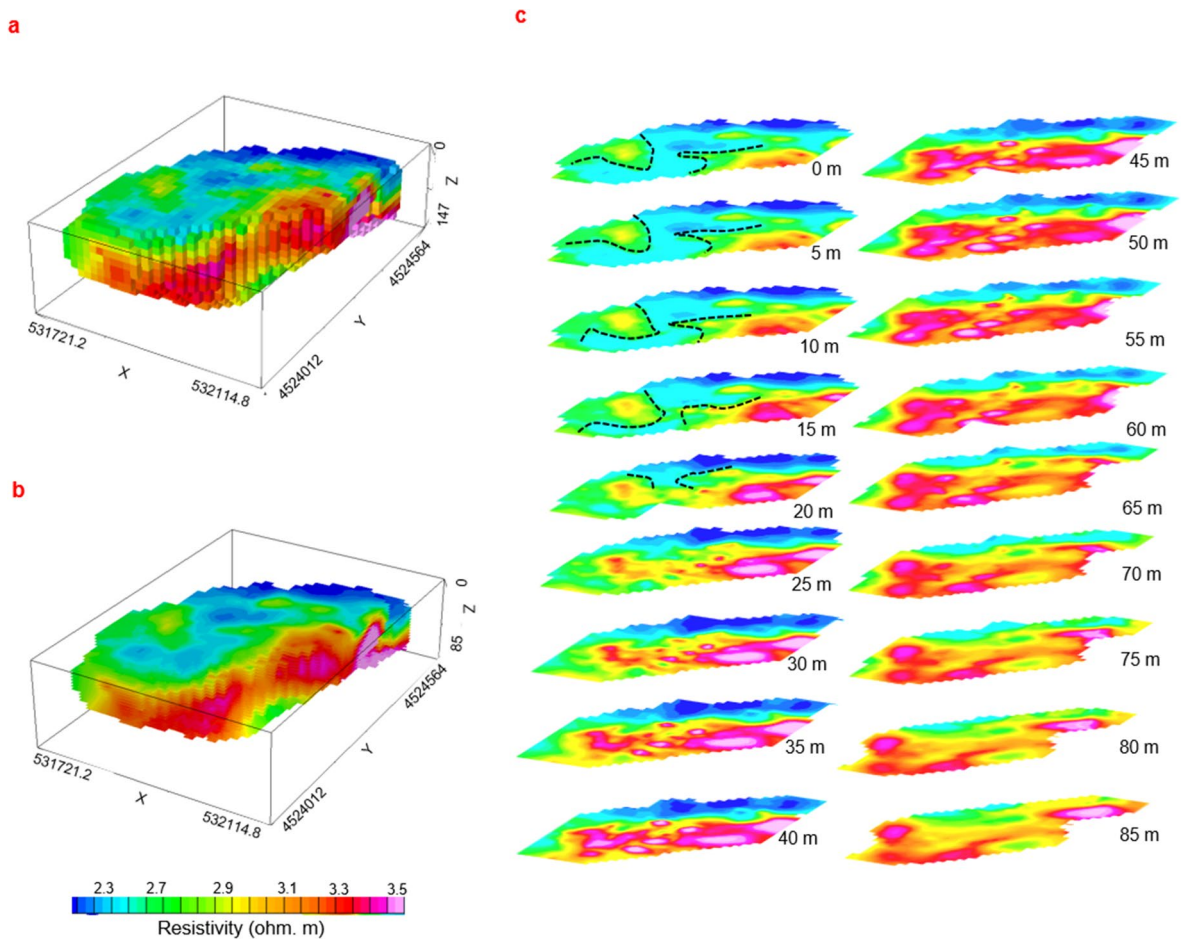


Fig. 11 3-D ERT images and level maps acquired from SF3, (**a**) 3-D ERT image acquired from SF3, (**b**) 3-D ERT image level maps displayed together, (**c**) 3-D ERT image level maps displayed every 5 m

Table 2 Measurement information of SRT data obtained from all study fields (SF1, SF2, and SF3) identified in Şahinkaya Member

Study Fields	Profile name/ Orientation	Profile Length (m)	Receiver Spacing (m)	Time Sampling (ms)	Recording Length (sn)	Vertical Stack
SF1	SRT1_P1-P4/NW-SE	106	2	0.25	0.5	3
	SRT1_P5-P6/ NE-SW	106	2	0.25	0.5	3
SF2	SRT2_P1/NE-SW	106	2	0.25	0.5	3
SF3	SRT3_P1-P10/ NE-SW	106	2	0.25	0.5	3
	SRT3_P11-915/ NW-SE	106	2	0.25	0.5	3

Table 3 Measurement information of MSAW data obtained from all study fields (SF1, SF2, and SF3) identified in Şahinkaya Member

Study Fields	Profile name/ Orientation	Profile Length (m)	Receiver Spacing (m)	Time sampling (ms)	Recording length (sn)	Vertical Stack
SF1	MASW1_P1-P4/ NW-SE	56	2	0.5	1	3
	MASW1_P5-P6/ NE-SW	56	2	0.5	1	3
SF2	MASW2_P1-P2/ NE-SW	56	2	0.5	1	3
SF3	MASW3_P1-P10/ NE-SW	56	2	0.5	1	3
	MASW3_P11-P15/ NW-SE	56	2	0.5	1	3

massive zones. In Fig. 9c, the regions with resistivity value of ~2995 ohm.m represent massive regions, and regions with high resistivity (~5838 ohm.m) represent possible karstic voids.

Figure 10a represents the 3-D ERT image obtained from SF1, Fig. 10b shows the combined image of the level maps of the 3-D ERT image, and Fig. 10c displays the level maps for the 3-D ERT image at 5 m intervals from the surface.

Table 4 Measurement information of GPR data obtained from all study fields (SF1, SF2, and SF3) identified in Şahinkaya Member

Study Fields	Profile name / Orientation	Profile Length (m)	Trace sampling interval (m)	Time-sampling interval in a trace (ns)
SF1	GPR1_P1-P16/P18 / NW-SE	11–80 m	0.025	0.14
	GPR1_P17/P19/ NE-SW	32–54 m	0.025	0.14
SF2	GPR2_P1/ NE-SW	90 m	0.025	0.14
SF3	GPR3_P1-P39/ NE-SW)	11–64 m	0.025	0.14
SF3	GPR3_P40-P49/ NW-SE)	11–54 m	0.025	0.14

The values given on the level maps represent depth values relative to sea level. When examining the level maps in Fig. 10c, there is a region of low resistivity (shown by dashed black lines) extending to a depth of 50 m and gradually decreasing in diameter as it goes deeper. This region is interpreted to indicate the underground extension of a sinkhole in the NE-SW direction. Furthermore, there are high resistivity values converging in the SE from height levels of ~10 to 95 m. This region is associated with massive bedrock. The highly resistive areas are thought to represent karstic voids within massive bedrock.

Figure 11a represents the 3-D ERT image obtained from SF3, Fig. 11b shows the combined image of the level maps of the 3-D ERT image, and Fig. 11c displays the level maps for 3-D ERT image every 5 m. In Fig. 11c, the low-resistivity region indicated by dashed black lines on the surface extends towards the NE-SW direction. These low-resistivity regions indicate the extension directions of sinkholes in the study field. This structure is visible to a depth of ~22 m. In addition, the resistivity values also increase as the depth level increases in the level maps. These regions represent massive bedrock considering the geology of the study area.

The SP graphs obtained from SF1, SF2, and SF3 are shown in Fig. 12. According to the study by Robert et al. (2011), SP values in water-saturated areas are known to decrease in the negative orientation. Taking this into consideration, there is a 5 mV decrease in the SP1_P4 graph on Fig. 12a between 70 m and 90 m, a 10 mV decrease between 80 m and 140 m. There is a 7 mV decrease between 140 m and 270 m in the SP2_P1 graph of Fig. 12b, and a ~10 mV decrease between 30 m and 70 m and between 115 m and 145 m in the SP3_P8 graph of Fig. 12c. In addition, the SP1_4 and SP3_8 profiles indicated by black lines are supported by vertically intersecting profiles.

An SP map (Fig. 13a) was generated from the data obtained from all profiles in SF1. Different width closures are observed in areas where SP values (-3 mV to -7.5 mV) are very low when this SP map is examined. The negative SP values were concentrated in the NW-SE orientation. In addition, closures that form around relatively high SP values (represented in red colour) on the same map are noteworthy. These closures are thought to correspond to small-sized caves (Sarıbudak 2015) within the study area.

The SP map in Fig. 14a was generated to determine the distribution of areas where water could be present in the SP graphs for SF3. When examining this map, there are variations in the form of closures in areas where SP values are low (represented by blue colour) within the range of -6 mV to -13 mV. These values are thought to indicate the groundwater situation in the study area. Additionally, closures also exist around relatively high SP values (represented by red colour) on the same map. These closures are thought to correspond to small caves (Sarıbudak 2015) within the study area.

Figure 15a shows the NE-SW oriented SRT1_P3 velocity section obtained from SF1. Although the Vp velocity distribution is shown for ~30 m depth in the section, when ray paths are plotted, information can only be obtained to a depth of 20 m. A three-layer medium appears in this section. Studies in the literature indicate that the Vp velocity range of limestone is between 2800 and 7000 m/s (Lavergne 1986; Carpenter et al. 2003; Cueto et al. 2018). When the section is examined, a layer with an average Vp velocity of 820 m/s, starting at a minimum depth of 2 m and deepening further in certain parts of the section, is seen. This layer is thought to represent the overlying layer in the investigated medium. Below the first layer is the second thin layer (2–10 m) with an average velocity of 2130 m/s. There is a third layer with an average Vp velocity of 3200 m/s and thickness of 4–20 m under the second layer. A bowl-shaped extension towards the depth is seen between 40 and 90 m on the profile, which is thought to represent a sinkhole.

The SRT2_P1 (Fig. 15b) section obtained from SF2 corresponds to the range of ~277.5–457.5 m of the ERT2_P1 profile (Fig. 8e) obtained from the same area. Figure 15b shows similar features to the section SRT1_P3 (Fig. 15a) obtained from SF1. Figure 14b shows a four-layered underground model with increasing velocity from the surface to the depths. These velocities are 820 m/s, 2130 m/s, 3200 m/s, and 4750 m/s, respectively from the surface to depth. A widening depression towards the depth is identified in this section.

The SRT3_P5 section with NW-SE orientation obtained from SF3 is shown in Fig. 15c. This area imaged ~30 m. The data ray paths only reach a maximum of ~20 m. Figure 15c presents a four-layered subsurface model with average Vp velocities of 820, 2130, 3200 and 4750 m/s, respectively.

Figure 16a shows the 3-D SRT image obtained from SF1, Fig. 16b shows a composite image of the level maps of the 3-D SRT image, and Fig. 16c shows the level maps

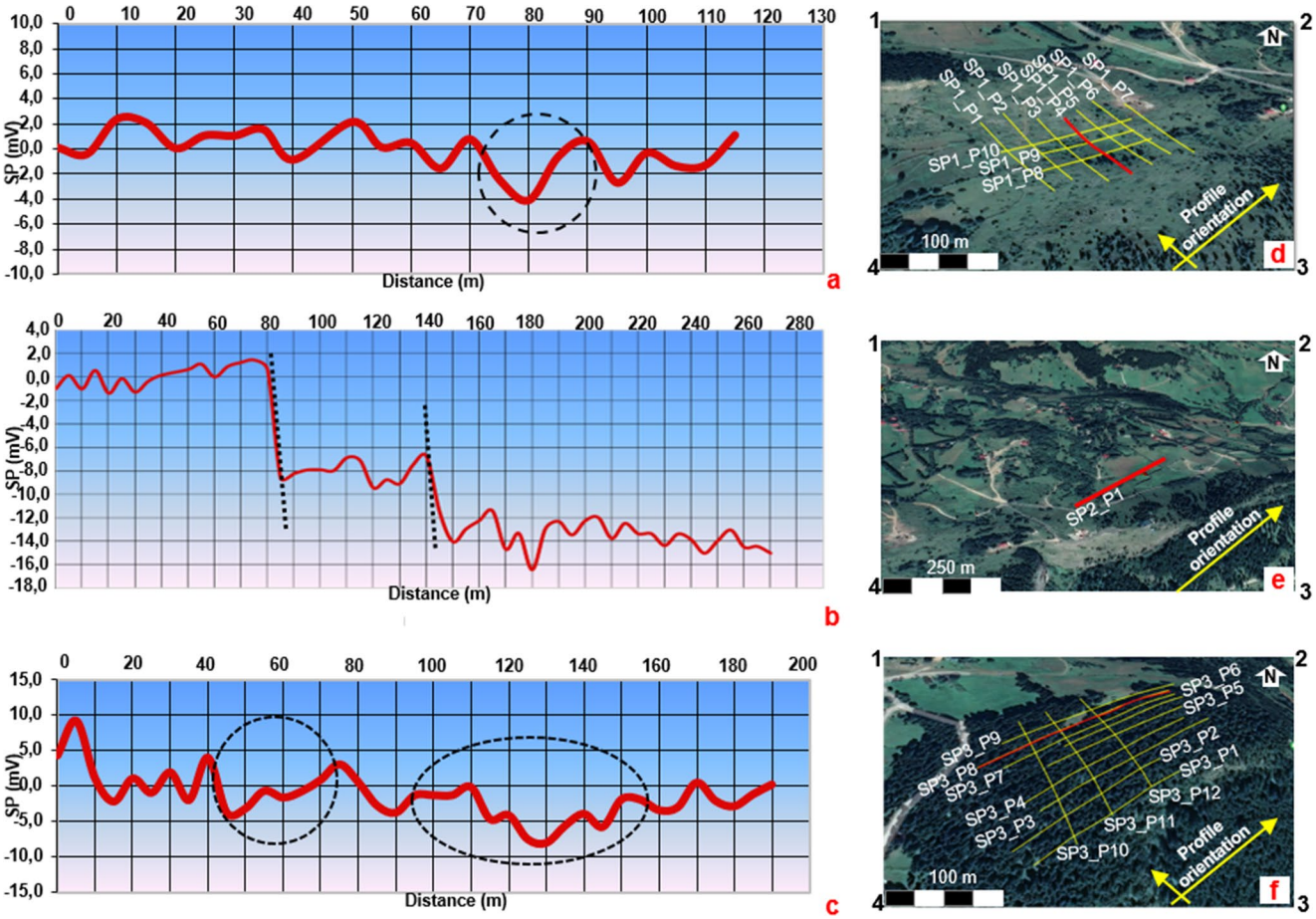


Fig. 12 SP graphs acquired from the Study Fields, (**a**) SP1_4 graph from SF1, (**b**) SP2_1 graph from SF2, (**c**) SP3_8 graph from SF3. Profiles (red lines) from which the graphs shown in a, b and c was acquired, are given (**d**) Application map of SF1 (coordinate of d: 1 = 40°51'38.36"N, 39°21'37.42"E; 2 = 40°51'39.70" N, 39°22'04.20"E; 3 = 40°51'20.67"N, 39°22'00.31"E; 4 = 40°51'21.73"N, 39°21'40.85"E), (**e**) Application map of SF2 (coordinate of e: 1 = 40°52'03.45"N, 39°21'35.42"E; 2 = 40°52'09.48"N, 39°22'34.66"E; 3 = 40°51'30.36"N, 39°22'20.46"E; 4 = 40°51'27.92"N, 39°21'54.88"E) and (**f**) Application map of SF3 (coordinate of f: 1 = 40°52'14.46"N, 39°22'32.88"E; 2 = 40°52'21.64"N, 39°22'53.98"E; 3 = 40°52'03.13"N, 39°22'49.82"E; 4 = 40°52'02.50"N, 39°22'36.96"E), respectively

of the 3-D SRT image for every 5 m. It is noteworthy that there is a low velocity region (black dashed lines) extending from 0 m to 20 m depth when the level map in Fig. 16c is examined. The diameter of this region decreases at depth. This region corresponds to the low resistivity zone (presumed to be a sinkhole) indicated by black dashed lines in the ERT sections (Fig. 10). Additionally, an increase in Vp velocity values was observed descending from the surface to deeper levels. The area characterised with high Vp velocity is thought to represent massive bedrock, considering the geological context.

Figure 17a shows the 3-D SRT image obtained from SF3, Fig. 17b shows a combination of level maps of the 3-D SRT image, and Fig. 17c shows the level maps of the 3-D SRT image for every 5 m. Going deeper from the surface, the variation in four different Vp velocity values represents different layers. Since the SRT data (Fig. 17c) collected from SF3 were obtained in the region considered to be the extension of doline on the 3-D ERT image in Fig. 11, the very low Vp velocity values at 0–10 m depths shown in Fig. 17c are considered to indicate the extension of the doline.

Figure 18a shows a Vs velocity-depth section obtained from the MASW1_P3 profile. The section represents a three-layered environment. The average velocity of the first layer is ~366 m/s, extending to 7 m. The second layer has a velocity of 605 m/s from 7 m to 24 m, while the third layer has a velocity of 1034.3 m/s and extends deeper than 24 m. The Vs 30 velocity is 561.7 m/s. Outcrops of rocks are often observed in SF1. SF1 has thin soil cover, and both field observations and geological studies confirm that the area is composed of limestones. Generally, limestones have high values for both Vp and Vs (Lavergne 1986). As seen from the Vs section (Fig. 18a), the velocity values are relatively high indicating that the study area consists of massive

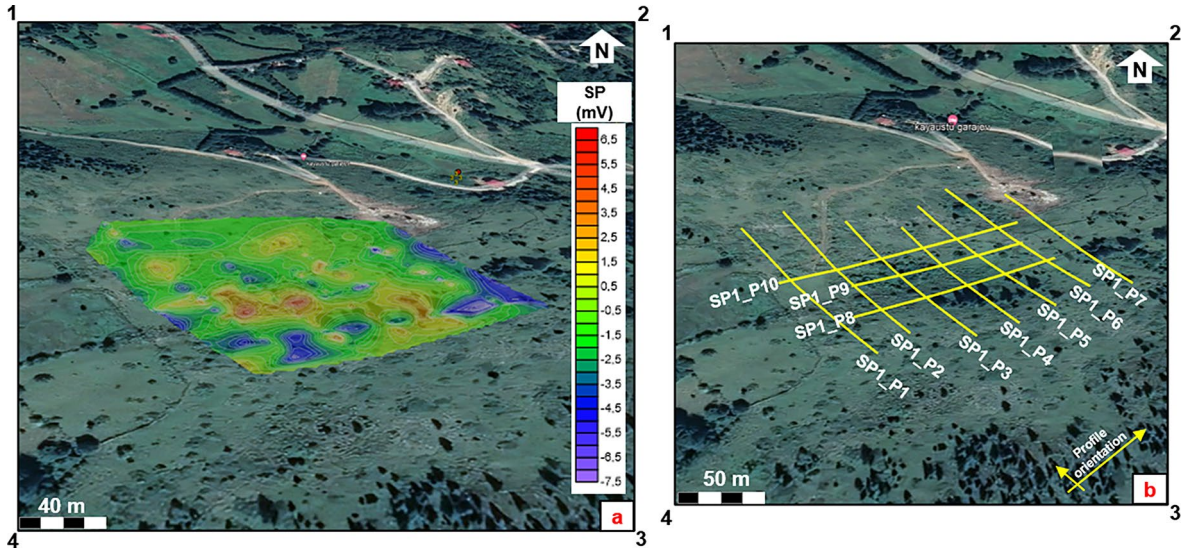


Fig. 13 SP profiles in SF1 and SP map generated from data from this profile. (**a**) SP map generated from SP data obtained from SF1 located in Şahinkaya Member (coordinate of a: 1 = 40°51'40.42"N, 39°21'38.95"E; 2 = 40°51'44.87"N, 39°22'06.47"E; 3 = 40°51'22.42"N, 39°22'01.63"E; 4 = 40°51'21.45"N, 39°21'48.81"E), (**b**) SP profiles in SF1 (coordinate of b: 1 = 40°51'36.44"N, 39°21'39.52"E; 2 = 40°51'39.48"N, 39°22'00.99"E; 3 = 40°51'20.66"N, 39°21'59.57"E; 4 = 40°51'20.61"N, 39°21'48.81"E)

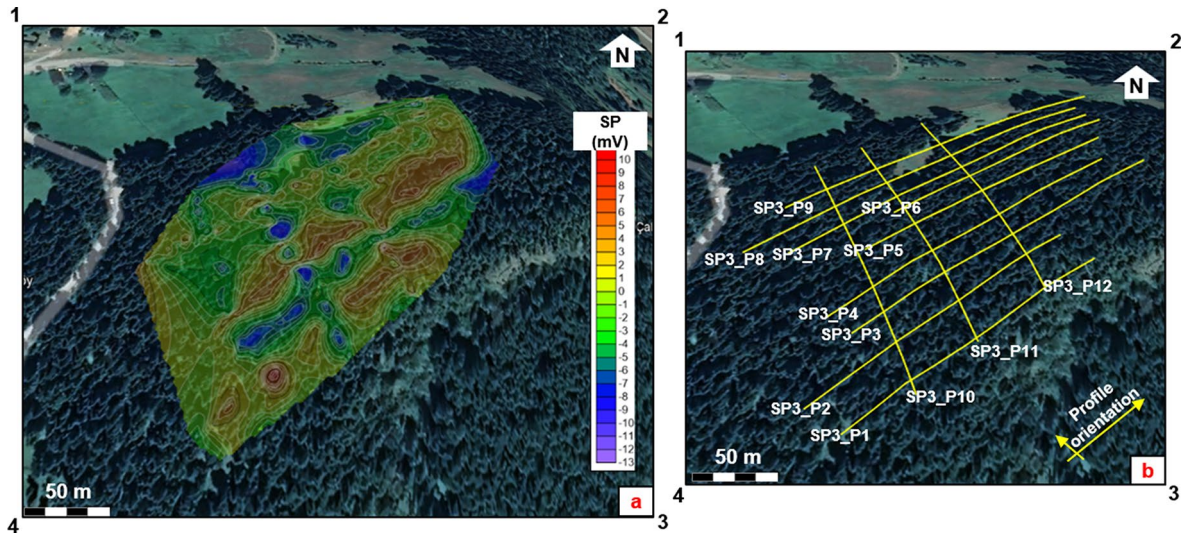


Fig. 14 SP profiles in SF3 and SP map generated from data from this profile. (**a**) SP map generated from SP data obtained from SF3 located in Şahinkaya Member (coordinate of a: 1 = 40°52'15.79"N, 39°22'33.59"E; 2 = 40°52'28.22"N, 39°22'00.12"E; 3 = 40°52'02.68"N, 39°22'47.96"E; 4 = 40°52'02.40"N, 39°22'37.58"E), (**b**) SP profiles in SF3 (coordinate of b: 1 = 40°52'15.52"N, 39°22'34.98"E; 2 = 40°52'22.25"N, 39°22'50.79"E; 3 = 40°52'02.39"N, 39°22'45.98"E; 4 = 40°52'02.30"N, 39°22'38.90"E)

or poorly weathered rocks. There are no indications of water content or voids in the Vs section.

The Vs velocity-depth section obtained from the MASW2_P1 profile in SF2 is shown in Fig. 18b. A three-layered environment is observed in this section. The first layer has an average velocity of ~370.5 m/s and extends to a depth of 9 m. The velocity of the second layer is 708.1 m/s and ranges from 9 to 25 m, while the third layer has a velocity of 949.6 m/s. The Vs 30 velocity of the environment is 584.1 m/s. This study area is similar in structure to SF1, but the velocities are relatively lower. However, the presence of a massive medium is particularly noticeable after 25–30 m.

In Fig. 18c, the Vs velocity-depth section obtained from the MASW3_P5 profile also shows a three-layered environment, similar to the other study fields. The first layer has an average velocity of ~439.6 m/s and extends to a depth of 9 m. The velocity of the second layer is 886 m/s and ranges from 9 to 24 m, while the third layer has a velocity of

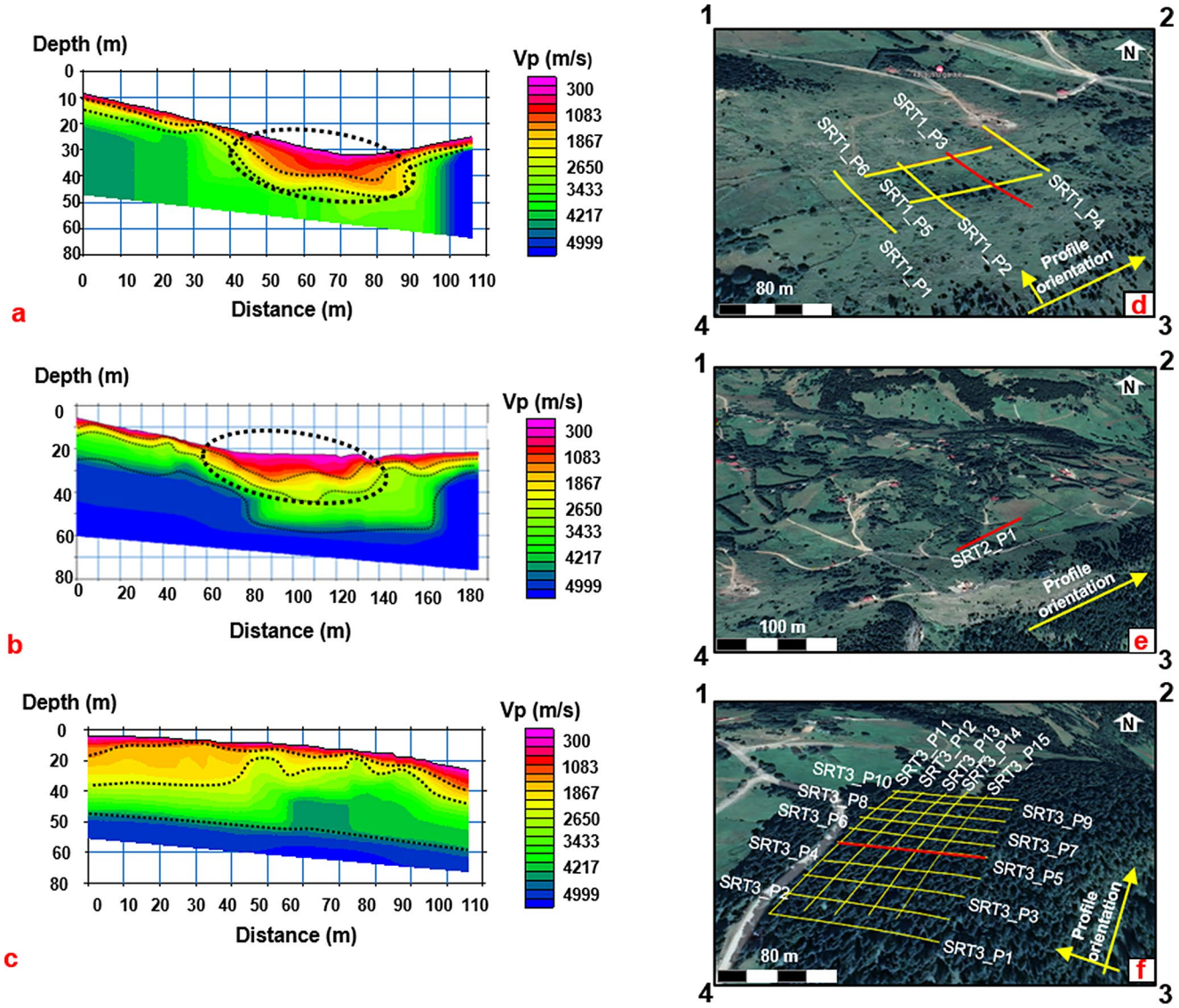


Fig. 15 SRT sections acquired from the Study Fields, (**a**) SRT1_3 section from SF1, (**b**) SRT2_1 section from SF2, (**c**) SRT3_5 section from SF3. Profiles (red lines) from which the sections shown in a, b and c was acquired, are given (**d**) Application map of SF1 (coordinate of d: 1 = 40°51'38.36"N, 39°21'37.42"E; 2 = 40°51'39.70"N, 39°22'04.20"E; 3 = 40°51'20.67"N, 39°22'00.31"E; 4 = 40°51'21.73"N, 39°21'40.85"E), (**e**) Application map of SF2 (coordinate of e: 1 = 40°52'00.16"N, 39°21'35.65"E; 2 = 40°52'04.66"N, 39°22'18.91"E; 3 = 40°51'30.16"N, 39°22'13.53"E; 4 = 40°51'28.73"N, 39°21'52.839"E) and (**f**) Application map of SF3 (coordinate of f: 1 = 40°52'19.85"N, 39°22'28.72"E; 2 = 40°52'33.56" N, 39°22'57.53"E; 3 = 40°52'03.54"N, 39°22'47.55"E; 4 = 40°52'02.93"N, 39°22'36.83"E), respectively

1459.6 m/s. The Vs 30 velocity in the SF3 area is 816.8 m/s. This study field exhibits a similar structure to the other two areas, and the velocity values are significantly high.

In Fig. 19a, the GPR section of the NW-SE oriented GPR1_P19 profile from SF1 is shown. This section was taken above a visible doline structure. When examining the GPR section, it is evident that the measured surface (red dashed line) exhibits a curved shape. The ~54 m long profile provides information from a depth of around 30 m. Five high-amplitude reflective surfaces with varying thicknesses are observed within the section. Additionally, vertical high-amplitude reflection surfaces are evident in certain parts of the section. Based on previous studies by Honings (2022), these vertical reflection surfaces are assumed to represent newly-formed, small-scale discontinuities within the limestone. The units between the reflective surfaces in the GPR1_P19 section are interpreted to represent different facies zones (FZ1, FZ2, FZ3, FZ4, and FZ5). Facies zones are regions that differentiate based on sedimentological and biological criteria across shelf-slope-basin sections (Flügel 2010; Consorti and Köroğlu 2019). In this study, the term facies zone (FZ) is used to represent limestone between

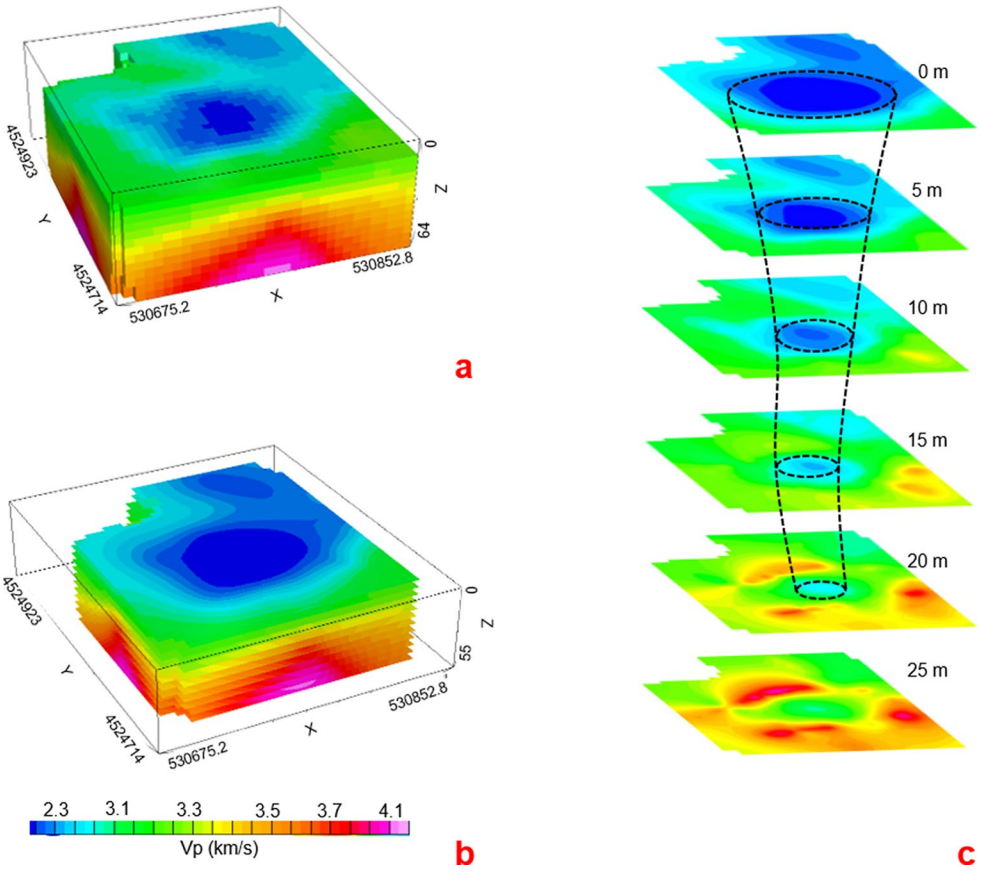


Fig. 16 SF1, 3-D SRT images and level maps, (a) 3-D SRT image acquired from SF1, (b) 3-D SRT image level maps displayed together, (c) 3-D SRT image level maps displayed every 5 m

boundaries in both geophysical and geological contexts, as opposed to the definition in Flügel (2010).

The GPR section (Fig. 19b) corresponds to the 355–540 m range of the ERT profile shown in Fig. 8b. In GPR2_P1 section, a hyperbolic reflection (shown by a yellow ellipse) is observed at a depth of 9 m from the surface.

The GPR3_P32 section (Fig. 19c) was taken approximately along a 23 m section of the ERT3_P8 (Fig. 8a) profile within SF3. The presence of two distinct reflection boundaries is noteworthy in this section. These reflection boundaries are interpreted to show different facies zones (FZ1, FZ2, and FZ3) within the area. The thicknesses of the facies zones between the interfaces are ~2, 2–14, and 14–30 m from the surface to depth (Fig. 19c). Each area between these interfaces represents different geological facies units. Additionally, inclined reflective interfaces are observed in different parts of the GPR3-P32 section. When the study by Koster and Kruse (2016) is examined, these reflective surfaces may indicate fractures in the limestone.

Şahinkaya Member: petrography, petrophysics and rock mechanic data

In addition to the geological (stratigraphy, palaeontology, and lithology) and geophysical features (Köroğlu and Kandemir 2019b; Consorti and Köroğlu 2019; Alemdağ et al. 2022, 2023) of the Şahinkaya Member described in previous sections, petrographic, petrophysical, and rock mechanic data are included in this section to further elaborate on the origin of karstification (Figs. 20 and 21; Tables 5 and 6).

Samples obtained from cores in the Şahinkaya Member (Fig. 20) were imaged at both macro- (DSLR camera using a macro lens) and micro-facies scale (petrographic microscopy X4 zoom) and with SEM (Fig. 21) to observe textural and structural features in detail (Table 5). Micro and macro structures, grain size components, and surface conditions of grains suitable for karstification in the facies were identified (Fig. 21). Although the samples are bioclastic facies (Table 5), texturally dense void ratios and signs of dissolution were not observed (Fig. 21). In addition to mechanical and hydrological effects causing karstification, fracture and fault systems in the sedimentary units are thought to have developed in parallel with the tectonic history of the region, resulting in the formation of dolines and caves, as well as the effects of volcanism given the post-Palaeogene

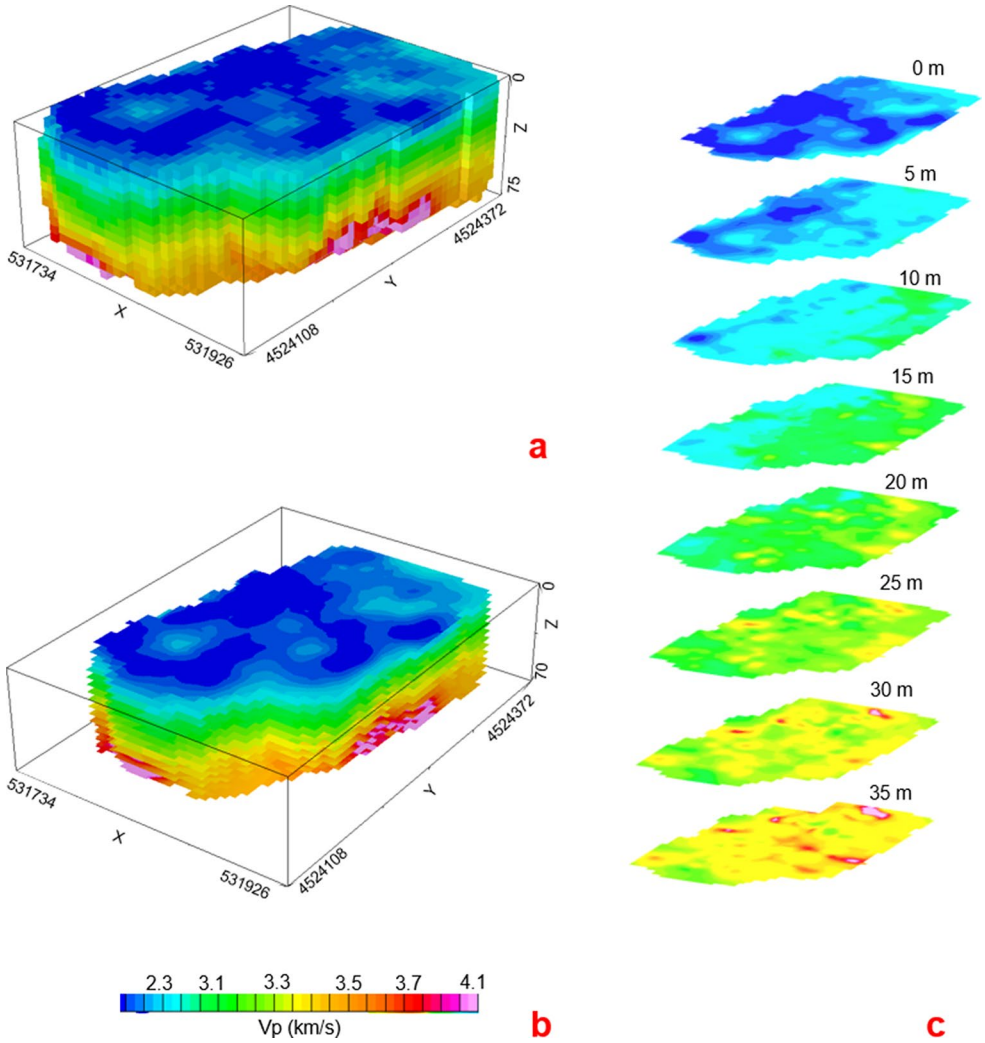


Fig. 17 SF3, 3-D SRT images and level maps, (a) 3-D SRT image acquired from SF3, (b) 3-D SRT image level maps displayed together, (c) 3-D SRT image level maps displayed every 5 m

age (Bektaş et al. 1995; Aydin et al. 2008; Yücel et al. 2014; Hippolyte et al. 2015; Consorti and Köroğlu 2019).

In basement and cover rocks, sedimentary components characterised by porosity and permeability are described as (a) unconsolidated/semi-lithified sands, (b) sandstone, and (c) carbonates (limestone and dolostone) (Halliburton 2001; Schlumberger Oilfield Glossary 2023). A detailed description of the lithology, facies, and rock fabric was made for the entire rock core to assign petrophysical measurements to the various rock properties (Archie 1952; Flügel 2010; Anovitz and Cole 2015). Carbonate rocks are classified into groups with different grain and particle/component sizes, and bioturbation, fissures, and micro-macro porosity are important for weathering properties and durability of limestone, dolomitic limestone, and travertine (Dunham 1962; Folk 1962, 1974; Embry and Klovan 1971; Lucia and Conti 1987; Lucia 1995, 2004, 2007; Pentecost 2005; Flügel 2010; Anovitz and Cole 2015; Nasri et al. 2019).

Rock type (for classification) is probably the most commonly-used descriptor of rock origin and structure (Deere and Miller 1966; Barton et al. 1974; ISRM 1981; Bieniawski 1989). Terminologically, igneous-volcanic, sedimentary, and metamorphic basic rock groups encompass a wide range of geological-mineralogical-mechanical factors with properties (mineral size and composition, degree of alteration, texture and structure, anisotropy, etc.) used in both sedimentology and other related disciplines (Palmström 1996). Limestone, one of the sedimentary rocks, is included in the behavioural classification under "*I. Crystalline texture*" within 4 rock groups and falls under the subheading "*A. Soluble carbonates and salts*" (Goodman 1989).

Table 6 lists both the rock classification and the mechanical properties of the samples from 3 to 7 m depth in borehole-2. When the petrographic details (Fig. 21) and the rock parameters are evaluated together, the rock class is "*R5: Very strong rock*" (Table 6). At the same time, the porosity and permeability values (Table 6) are very low compared to the average for packstone-grainstone-rudstone limestone (Table 5; Fig. 21) (Dunham 1962; ISRM 1981; Flügel 2010).

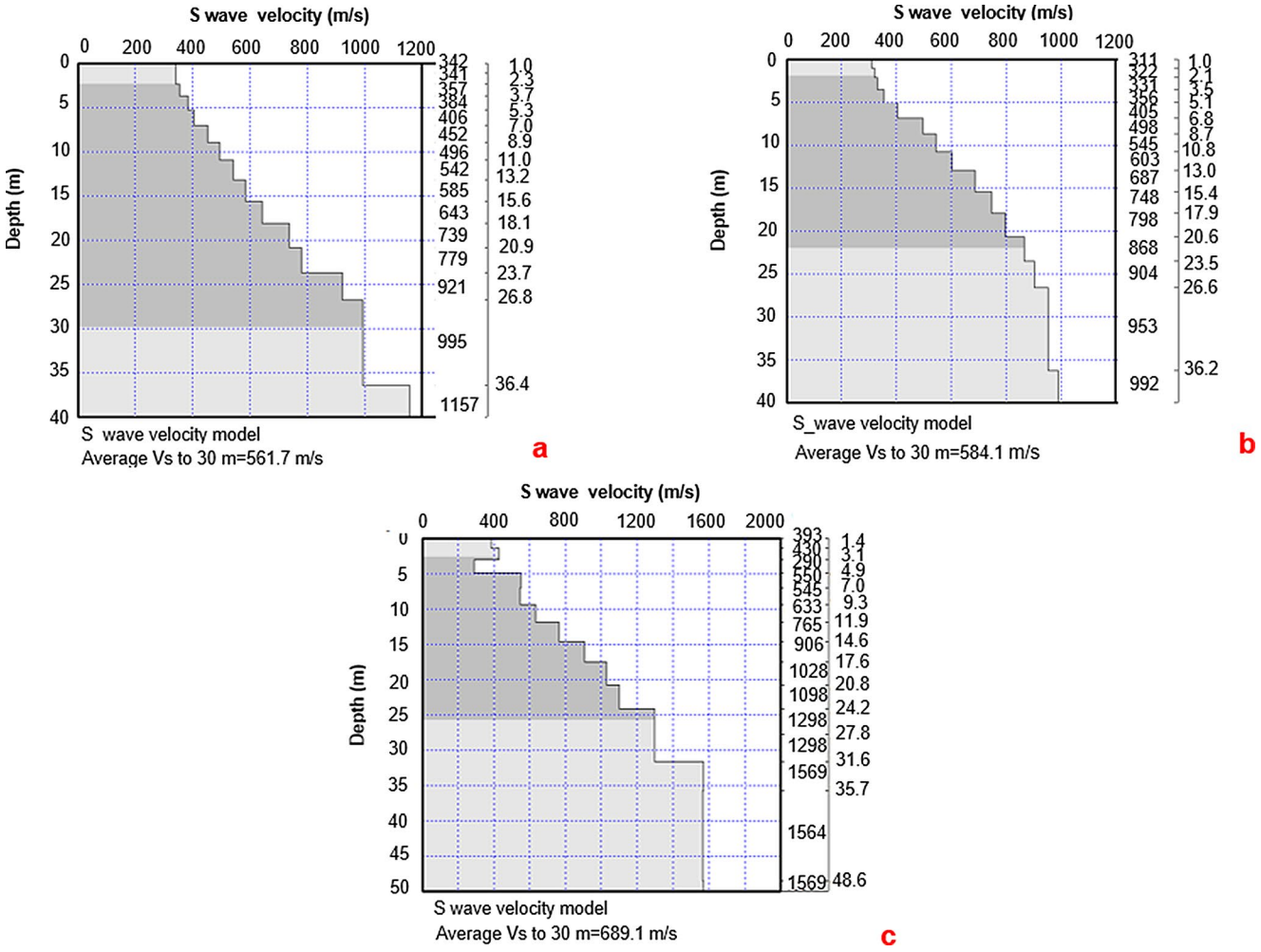


Fig. 18 S-wave velocity-depth sections obtained from the study fields, (**a**) S-wave velocity-depth section of MASW data from SF1, (**b**) S-wave velocity-depth section of MASW data from SF2, (**c**) S-wave velocity-depth section of MASW data from SF3.

Before core analysis, drill core plug samples were stored in alcohol in a vacuum-controlled oven to remove possible formation water and drilling wastes. As part of basic core analyses, the length, diameter, and weight of the drill core plugs were first measured (Table 7). A 'helium porosimeter' was used to measure porosity, and pore volume was calculated from the pressure drop due to void volume inside the plug using Boyle and Charles laws (TPAO https://www.tpao.gov.tr/file/2203/tpao-arge-hizmet-katalogu-2022-7636245b24701e05.xlsx). At this stage, the grain density was also calculated based on pore volume. Permeability was measured by passing dry air through the sample located in a 'Hassler' type core cell and calculated using Darcy's law (Darcy 1856). The measured air permeability values (kair) were converted to equivalent liquid permeability values (kL) using the Klinkenberg correction (TPAO https://www.tpao.gov.tr/file/2203/tpao-arge-hizmet-katalogu-2022-7636245b24701e05.xlsx).

Limestone formations vary greatly in thickness, density, porosity, and permeability (Table 7), and spaces in limestone can range from microscopic original pores to large fractures and caves that form subsurface channels (Bear 1972; Ofluoğlu 1993; Törk et al. 2013; Köroğlu and Kandemir 2019b). Water tends to expand limestones by dissolving them along fractures and cracks, increasing permeability and porosity in microstructures over time (Bear 1972; Flügel 2010). Eventually, the limestones of the Şahinkaya Member were transformed into a region characterised by karst structure and texture (the underground distribution of sinkholes is shown in Figs. 5, 6, 7, 8, 9, 10, 11, 12 and 15, 16, 17 shows the area where the short extension of Çal Cave is cut; Fig. 19 shows the boundaries of the facies zones, and Fig. 19c shows fractures/cracks within the Şahinkaya Member; Figs. 12, 13, 14 shows parts with high water content) (Ofluoğlu 1993; Törk et al. 2013; Köroğlu and Kandemir 2019b).

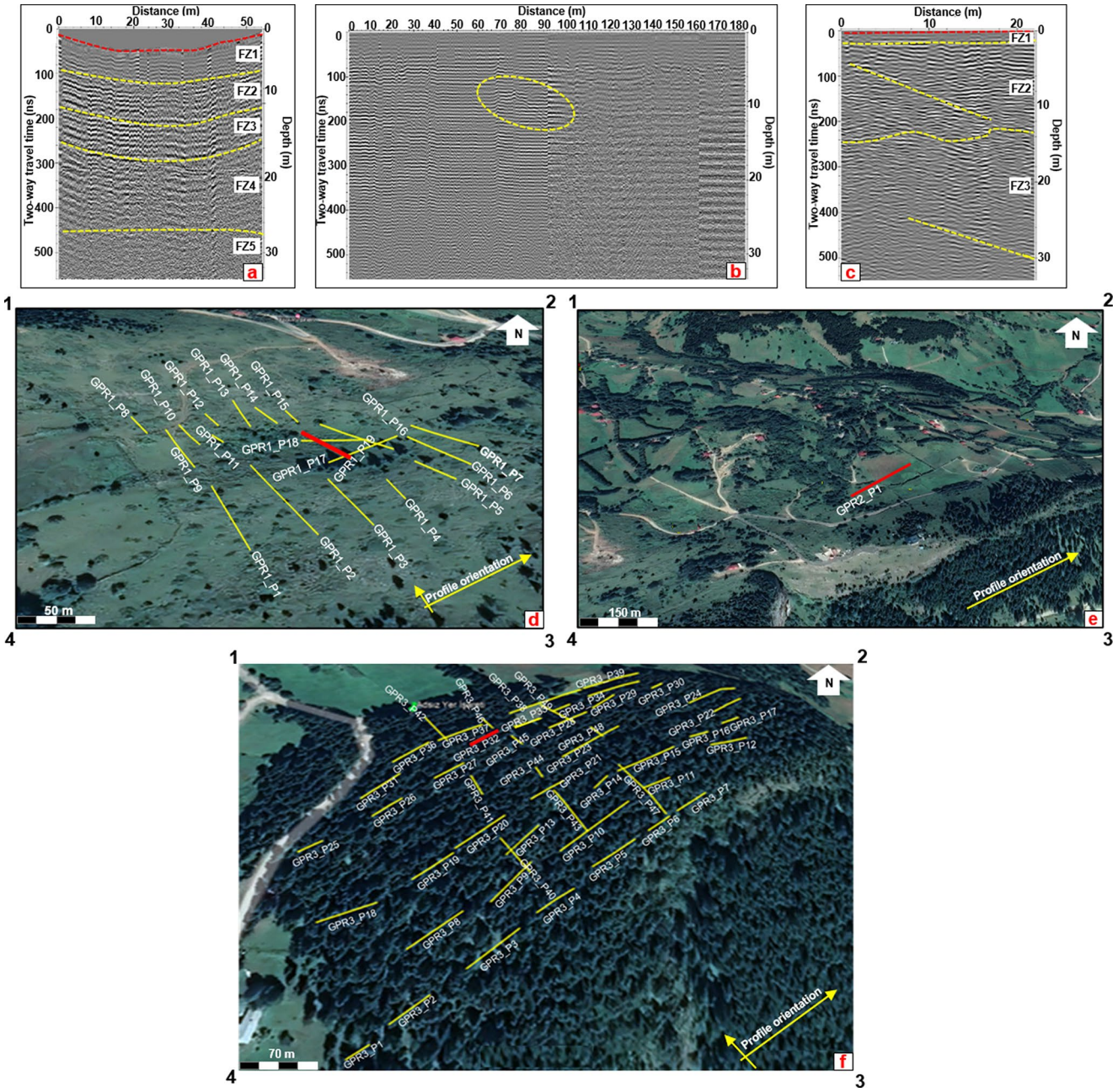


Fig. 19 GPR sections acquired from the Study fields, (**a**) GPR1_P19, (**b**) GPR2_P1, **c**) GPR3_P32 sections. Profiles (red lines) from which the sections shown in a, b and c was acquired, are given (**d**) Application map of SF1 (coordinate of d: 1 = 40°51'31.21''N, 39°21'43.81''E; 2 = 40°51'33.29''N, 39°22'00.51''E; 3 = 40°51'21.15''N, 39°22'00.88''E; 4 = 40°51'22.04''N, 39°21'48.15''E), (**e**) Application map of SF2 (coordinate of e: 1 = 40°52'01.87''N, 39°21'35.65''E; 2 = 40°52'06.64''N, 39°22'37.24''E; 3 = 40°51'30.88''N, 39°22'24.62''E; 4 = 40°51'27.39''N, 39°21'55.76''E) and (**f**) Application map of SF3 (coordinate of f: 1 = 40°52'13.50''N, 39°22'32.20''E; 2 = 40°52'22.44'' N,39°22'55.45''E; 3 = 40°52'04.73''N, 39°22'52.33''E; 4 = 40°52'03.03''N, 39°22'36.90''E), respectively

Discussion

Within the scope of this study, hydrogeophysical studies were conducted for the first time in the Şahinkaya Member to reveal the 2-D and 3-D subsurface structure of the investigated areas (SF1, SF2 and SF3). When the findings obtained from ERT, SP, SRT, MASW, and GPR data are examined, the ERT results (Fig. 8) show the locations of karstic voids and areas with high water content more prominently (in terms of depth, resolution, shape, etc.) when compared to the other methods (SP, SRT, MASW, and GPR). The data from maximum depth (~120 m) was obtained from the 600 m long ERT2_P1 (Fig. 8b) section in SF2. Areas showing low SP values (represented by blue colour)

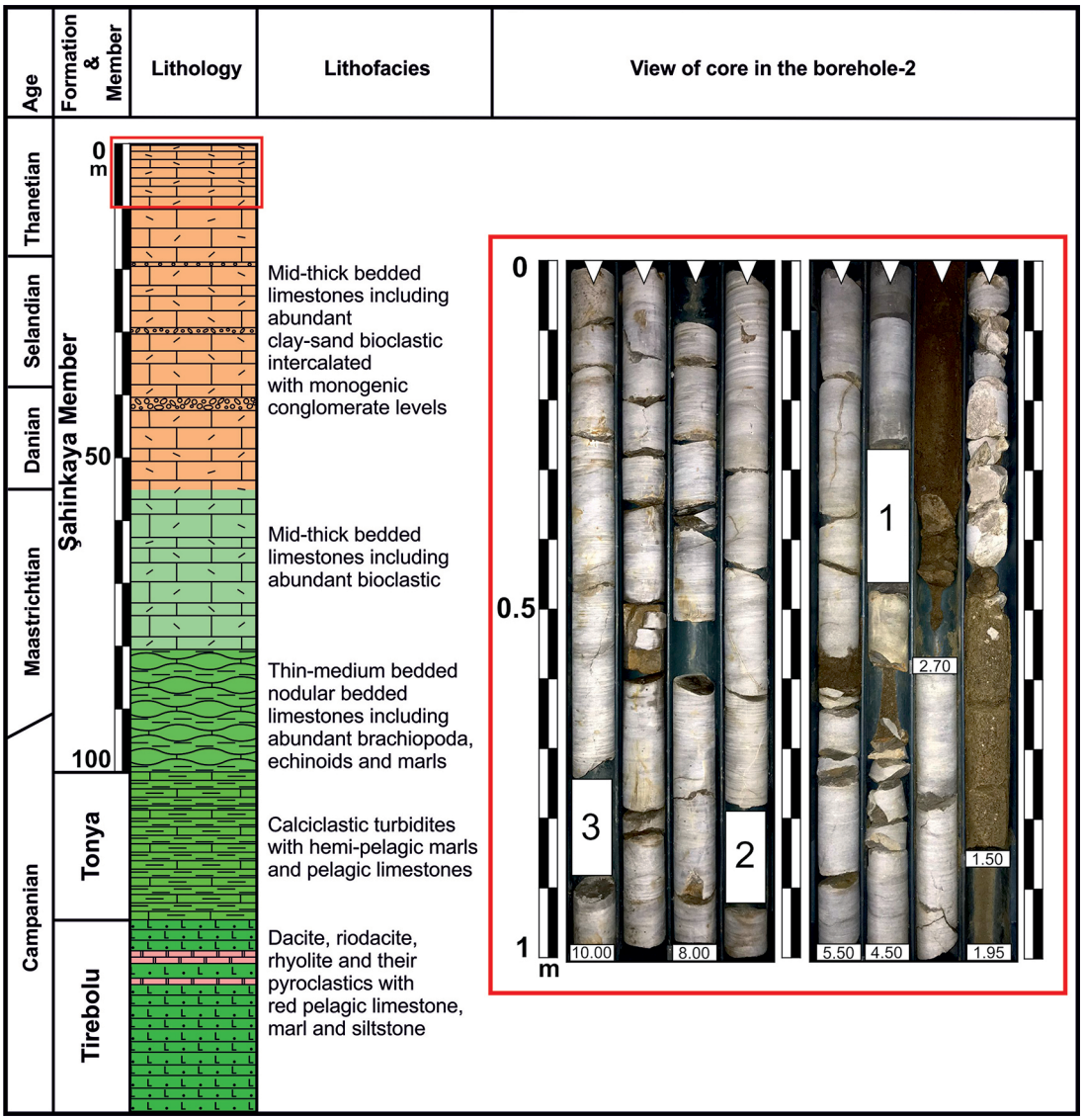


Fig. 20 Generalized stratigraphic column section of the Düzköy (Trabzon). (modified from Köroğlu 2018; Köroğlu and Kandemir 2019b; Consorti and Köroğlu 2019) and cores from borehole-2 of the Şahinkaya Member

with varying closures are considered to be indicators of groundwater conditions according to Hasan et al. (2019), when examining the SP maps (Figs. 13a and 14a) generated from SP data (Fig. 12). In addition, closures around relatively high SP values (represented in red) in these maps are thought to correspond to small size caves, taking into account the studies by Sarıbudak (2015) and Vichabian (2002). A four-layered subsurface model was identified for the study fields by considering the Vp velocity distributions obtained from the SRT sections (Fig. 15). Since the velocity values obtained from the SRT sections increase from the surface to depth, the uppermost layer may consist of highly weathered material, while the lower layers may be composed of less weathered or massive rocks. In addition, the underground extensions of the sinkholes were also detected in the 3-D images (Figs. 16 and 17) obtained from the SRT sections, similar to the study by Jabrane et al. (2023). The Vs velocity depth model obtained from MASW data was used to determine the layer thicknesses. As in the study by Lejzerowicz et al. (2018) of radar facies, high amplitude reflection signals from different lithologic layer boundaries were recorded using the GPR method. In the GPR sections, distinct reflections were observed at the boundaries of FZ at various depth levels, reaching a depth of 32 m within the Şahinkaya Member (Fig. 19). Also, the inclined reflections detected in GPR3_P32 section (Fig. 19c) were interpreted as the presence of fractures/cracks within the limestone.

When examining the ERT1_3 and SRT1_3 results within SF1, the underground extension of the sinkholes observed at the surface continued in the NE-SW orientation.

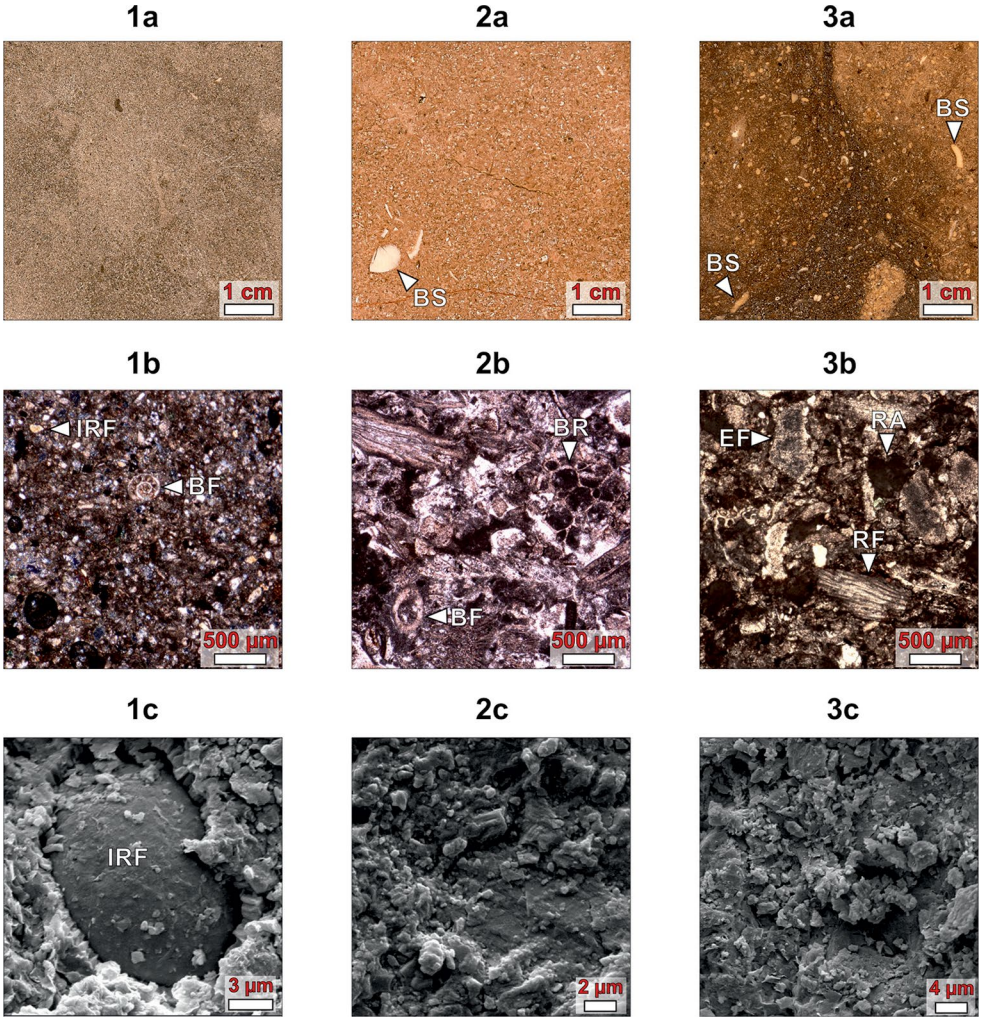


Fig. 21 Petrographic of Şahinkaya Member and the limestone cores (sample levels are shown in the core box in Fig. 19) with different features detailed images (DSLR: Digital Single-Lens Reflex, Polarization Microscopy, SEM: Scanning Electron Microscope). S.N-1: 1a. macro-facies, 1b. micro-facies (BF: Benthic Foraminifera, IRF: Igneous Rock Fragments), 1c. SEM (IRF: Igneous Rock Fragments, microstructure of granular/crystalline calcitic texture); S.N-2: 2a. macro-facies (BS: Bioclastics), 2b. micro-facies (BF: Benthic Foraminifera, BR: Bryozoa), 2c. SEM (microstructure of granular/crystalline calcitic texture); S.N-3: 3a. macro-facies (BS: Bioclastics), 3b. micro-facies (EF: Echinodermata Fragments, RA: Red Algae, RF: Rudist Fragments), 3c. SEM (microstructure of granular/crystalline calcitic texture)

Table 5 Macro-facies (Tucker and Wright 1990; Flügel 2010), micro-facies (Dunham 1962; Embry and Klovan 1971; Flügel 2010), and SEM image descriptions of borehole-2

S. *N*	Macro-Facies (Fig. 21)		Micro-Facies (Fig. 21)		SEM (Scanning Electron Microscopes) (Fig. 21)	
1	a	Allochthonous limestone: grey-beige coloured; fine-grained; well-sized; sparsely observed macroscopic fossil fragments; homogeneously texture	b	Packstone-grainstone: Bioclastic with benthic foraminifera; igneous rock fragments (sand-sized etc.); red algae and components derived from the neritic environment	c	Microstructure of granular/crystalline calcitic texture
2	a	Allochthonous limestone: yellow-orange coloured; fine- to medium-grained; medium- to well-sized; macroscopic fossil fragments; hemi-homogeneous texture	b	Grainstone-rudstone: Bioclastic with benthic foraminifera; igneous rock fragments (sand-sized etc.); red algae, bryozoa, coral and echinoid fragments and components derived from neritic environment	c	Microstructure of granular/crystalline calcitic texture
3	a	Allochthonous limestone: grey-brown-yellow coloured; fine-medium-coarse grained; medium-well size; macroscopic grains; heterogeneous texture	b	Grainstone-rudstone: Bioclastic with benthic foraminifera; igneous rock fragments (sand-sized etc.); red algae, bryozoa, coral and echinoid fragments and components derived from neritic environment	c	Microstructure of granular/crystalline calcitic texture

Additionally, the regions with low SP values were concentrated along the same orientation (NE-SW) on SP maps of the same area (Fig. 14). In a study conducted by Törk et al. (2013), the underground river and branch extensions of Çal Cave had the same orientation as the extent of the cave obtained from geophysical surveys conducted in this study. Since sinkholes are points where surface waters seep underground, the sinkholes within SF1 are sources that feed

Table 6 Experimental results of borehole-2 in Şahinkaya Member (Study Field 3) of TCR (Total Core Recovery) - RQD (Rock Quality Designation) - SCR (Solid Core Recovery), physical properties and Axial Compressive Strength, Çalköy (Düzköy/Trabzon) for the development plan of the area in the vicinity of geological and geotechnic survey report by Günan (2023)

Location X: 531908.04 Y: 4526144.00 Z: 1306 m UTM zone 37 N/ WGS 84	Depth (m)	TCR (%)	RQD (%)	SCR (%)	Lithology						Formation / Member
Borehole-2	0.00-1.50	53	0	0	Soil + Residual Clay						**Tonya / Şahinkaya**
	1.50–2.70	50	0	0							
	2.70–4.50	83	61	78	Gray-Beige Colour Clay-Sandy Bioclastic Limestone						
	4.50–5.50	100	60	90							
	5.50-8.00	80	64	80							
	8.00–10.00	100	80	100							
	Depth	**Diameter (D)**	**Height (H)**	**Volume (V)**	**Weight (W)**	**Density (ρ = W/V)**	**Sample Surface Area**	**Failure Load**	**Axial Compressive Strength**		**Rock Classification** ISRM (1981)
	m	**cm**	**cm**	**cm^3**	**g**	**ρ (gr/cm^3)**	**cm^2**	**kgf**	**kgf/cm^2**	**MPa**	**σ_c = (F/A)**
	3	6.33	6.33	199.20	535.18	2.69	31.47	33,096	1051.70	105.17	R5: Very strong rock
	7	6.32	6.32	198.26	530.94	2.68	31.47	33,889	1080.31	108.03	R5: Very strong rock

Table 7 Porosity and permeability values of the Şahinkaya Member according to the basic core analyses (analysed by TPAO-ARGE).

S. N	Depth	Diameter (D)	Height (H)	Weight (W)	Grain Density	Porosity	Permeability	
	m	mm	mm	gr	g/cm^3	%	kair md	kL md
1	4.50	37.61	67.99	200.37	2.68	1.14	< 0.1	< 0.1
2	5.50	37.68	67.30	195.72	2.67	2.33	< 0.1	< 0.1
3	10.00	37.56	69.04	200.32	2.65	1.35	< 0.1	< 0.1

the underground river flowing through Çal Cave, which is located along the same orientation as the sinkholes. Additionally, different FZ were revealed in the GPR sections obtained from this area. The Vp velocities measured in the SRT1_3 sections in this area indicate FZ variations. Furthermore, the inclined reflections observed in the GPR3_P32 sections are interpreted to represent fractures and cracks within the limestone. Due to the very thin first layer and its low Vp velocity in the SRT sections, the first and second layers appear to form one layer in the MASW sections.

When examining the results from integrated geophysical data obtained from the profile in SF2 in the NE-SW direction in Fig. 22, the high resistivity (4449 ohm.m) anomaly in the ERT section in Fig. 22a corresponds to the part where the natural potential difference suddenly decreases (from 0 mv to -8 mv) in Fig. 22b and the Vp (1344 m/s) and Vs (494 m/s) velocities are quite low in the SR (Fig. 22c) and MASW sections. In addition, the same anomaly presents as branch with hyperbolic reflection, indicated by the yellow ellipse in Fig. 22d. The depth and width of this anomaly were determined as ~60 m width and ~110 m depth in the ERT section (Fig. 22a). The dominant lithology in the study field of the Şahinkaya Member has a thickness of ~100 m, as determined from stratigraphic sections by Köroğlu (2018) and Consorti and Köroğlu (2019). According to this information, the common region showing anomalies on the different geophysical sections is thought to be an indication of a significantly large karst cavity within the Şahinkaya Member, rather than representing a different rock type. Additionally, based on the study conducted by Törk et al. (2013), the entrance of the cave is at an elevation of 1132 m, and the highest point (end of the short arm) is 52 m above the entrance elevation in the NE-SW direction. Therefore, the level at 1184 m represents the base of the cave. When examining the ERT section, the deepest part of the high-resistivity region in Fig. 22a, which is believed to

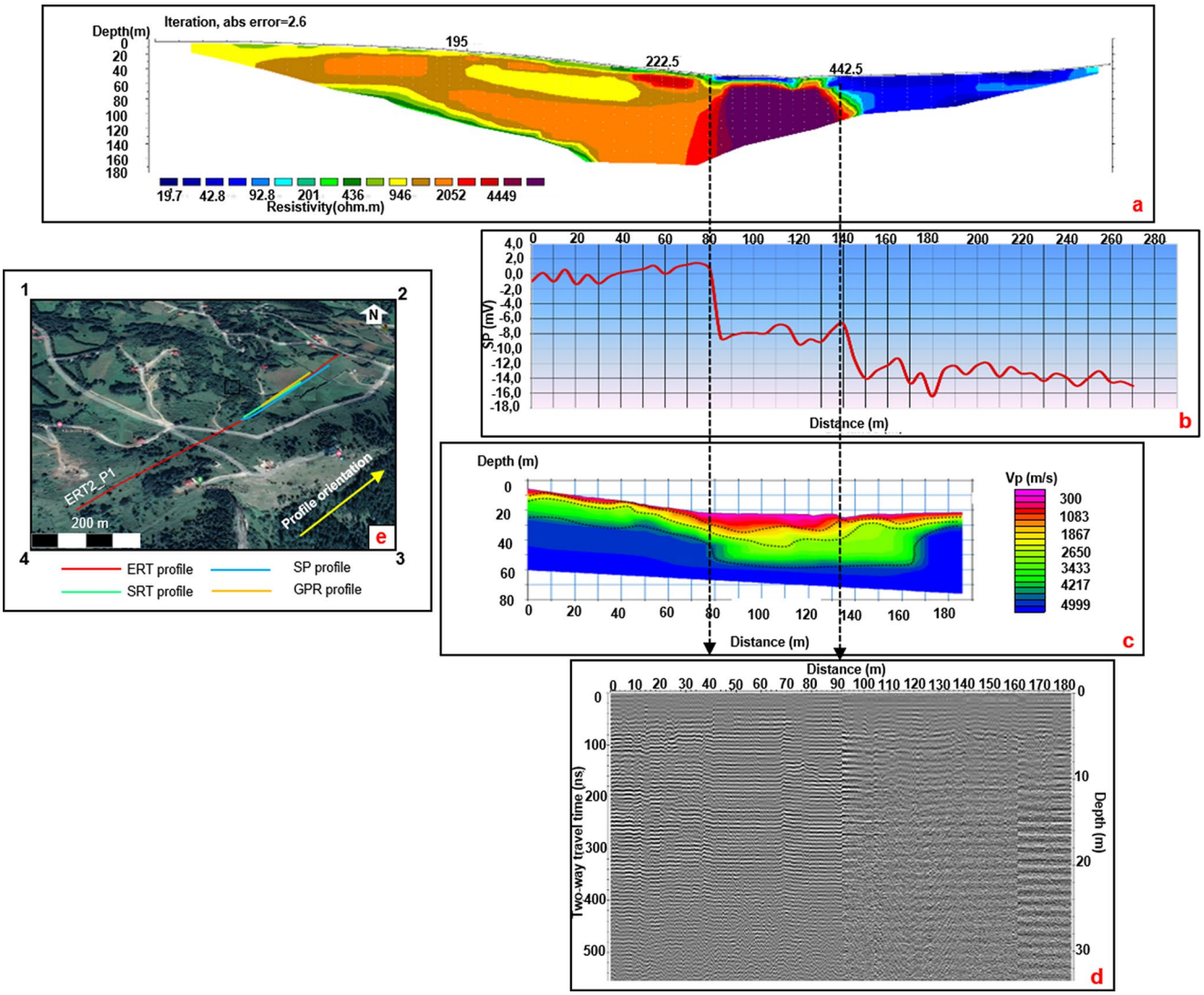


Fig. 22 ERT, SP, SRT and GPR sections from SF2. (**a**) ERT section, (**b**) SP graph, (**c**) SRT section, (**d**) GPR section, (**e**) Profile from which sections at a, b, c and d are obtained (coordinate of e: 1 = 40°51'47.28"N, 39°21'44.10"E; 2 = 40°51'44.76"N, 39°22'11.74"E; 3 = 40°51'26.77"N, 39°21'48.70"E) 4 = 40°51'25.18"N, 39°22'17.43"E;

be a karst cavity, reaches depths of up to 1180 m. Therefore, it can be concluded that the region believed to be a karst cavity corresponds to the short arm of the cave. In addition, the very low resistivity (51.7 ohm.m) region of the ERT section in Fig. 22a in the 420–600 m axis length range is thought to represent a water-saturated zone. The GPR section (Fig. 22d) for this area corresponds to the 90–180 m axis range of the profile. Therefore, this area, which manifests as a discontinuity in the lateral direction from 90 m, is interpreted to correspond to a region with very high water content.

Based on integrated geophysical surveys conducted in Çal-Camili Natural Park, which is located in SF3, the locations of underground karstic voids and the orientations of the dolines were determined. When examining the 2-D and 3-D ERT sections, the low-resistivity weathered zone, which is believed to represent the dolines, extends in the SE-NW direction. The higher resistivity regions on the right and left sides of the doline orientations are considered to represent massive bedrock. The very high resistivity zones within the massive rocks are thought to indicate karstic voids, considering their structural features. In the same images, some of the karstic voids are very close to the surface. It is of great importance for environmental hazards to identify these voids seen in karstic areas with geophysical and geological measurements before any building is constructed. Similar to the study by Cooper et al. (2011) of karst rock and all of its associated features, and development and environmental constraints on infrastructure in Great Britain.

When examining the 2-D and 3-D SRT results, the dolines extend in the SE-NW direction, similar to the ERT sections. It is believed that there is a layer at a depth of 2 m from the surface, which represents the cover layer, based on the SRT, MASW, and GPR sections. When analysing the SP maps, low SP values concentrate in the NE-SW direction. The dolines observed from the surface were determined to orient along this direction. Additionally, in the GPR sections obtained from this area, FZ of varying thicknesses were detected starting from the surface. Finally, the order of application of geophysical data that should be used when working in karst areas is given in Fig. 23 and explained in the conclusion section, taking into account all the results of this study.

Conclusion

In the specific context of this research, sinkholes (dolines), karstic voids, and water-saturated areas in limestones were identified by integrated geophysical methods, applied for the first time in Şahinkaya Member. Data from maximum depth were obtained by the ERT method in these areas. In addition, this method was an effective technique for determining the distribution of water-bearing zones, dolines, and karstic voids in limestones by utilising the differences in resistivity change. The SP method was also effective for determining water distribution and voids by utilising natural potential difference changes. SRT was an effective method for determining layer thicknesses and doline extent due to changes in Vp velocity values. Another application, GPR was a useful and effective method for identifying facies zones and fractures/cracks in limestones at shallow depths. Last but not least, the MASW method was an effective method for determining layer thicknesses due to changes in Vs velocity values.

Based on the results of the integrated geophysical (electrical resistivity tomography, self-potential, seismic refraction, multichannel analysis of surface waves, ground penetrating radar) data obtained from all study fields (SF1, SF2, and SF3), it is recommended to perform the geophysical methods in stages as depicted in the flow chart when investigating karstification and high-water content in karstic areas (Fig. 23).

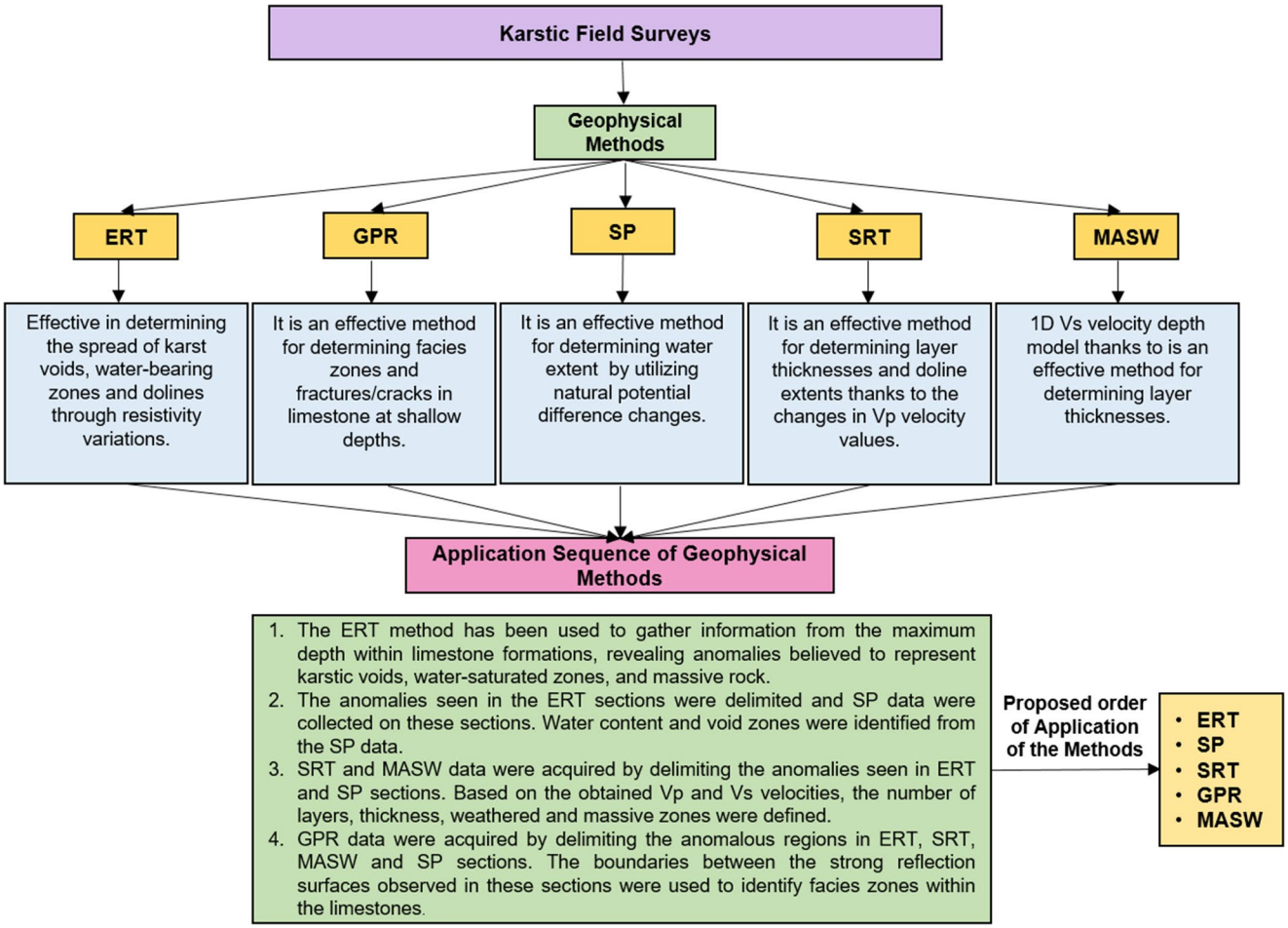


Fig. 23 The proposed application flow chart of geophysical methods in karstic areas

Supplementary Information The online version contains supplementary material available at https://doi.org/10.1007/s10064-024-03779-7.

Acknowledgements We would like to thank Dr. Merve Özyurt (Karadeniz Technical University, Trabzon), Dr. Oğuz Mülayim (TPAO, Adıyaman), Dr. Onur Alkaç (Fırat University, Elazığ), İsmail Günan (geologist, Trabzon), and Mustafa Şükrü Kulein (architect, Trabzon) for their contributions to data and laboratory study and the geological section of this study. We would like to thank Prof. Dr. Çağlayan Balkaya (Süleyman Demirel University, Isparta) for a review of the geophysical sections of this study. This study was funded by the Scientific and Technological Research Council of Türkiye (TÜBİTAK) under Project Number 121Y413.

Funding Open access funding provided by the Scientific and Technological Research Council of Türkiye (TÜBİTAK).

Open Access This article is licensed under a Creative Commons Attribution 4.0 International License, which permits use, sharing, adaptation, distribution and reproduction in any medium or format, as long as you give appropriate credit to the original author(s) and the source, provide a link to the Creative Commons licence, and indicate if changes were made. The images or other third party material in this article are included in the article's Creative Commons licence, unless indicated otherwise in a credit line to the material. If material is not included in the article's Creative Commons licence and your intended use is not permitted by statutory regulation or exceeds the permitted use, you will need to obtain permission directly from the copyright holder. To view a copy of this licence, visit http://creativecommons.org/licenses/by/4.0/.

References

Abdallatif T, Khafagy AB, Khozym A (2015) Geophysical investigation to delineate hazardous cavities in Al-Hassa Karstic Region, Kingdom of Saudi Arabia, vol 5. Engineering Geology for Society and Territory

Alemdağ H, Öğretmen Aydın Z, Köroğlu F, Şeren A, Babacan AE, Fırat Ersoy A (2022) Characterization of doline morphology by Electrical Resistivity Tomography (ERT) method: Example of Şahinkaya Member Çalköy, Trabzon/ Turkey, 74. Geological Congress of Turkey with international participation, Ankara, Türkiye.

Alemdağ H, Öğretmen Aydın Z, Köroğlu F, Şeren A, Babacan AE, Fırat Ersoy A (2023) Şahinkaya kireçtaşları içindeki dolinlerin, karstik boşlukların ve yeraltı su akış sisteminin hidrojeofizik yöntemlerle araştırılması: Çal Mağarası civarı Düzköy (Trabzon)/ Türkiye, ÇAYDAG, 121Y413, TÜBİTAK, Ankara, Türkiye (in Turkish with English abstract).

Andrej M, Uros S, Studies K (2012) Electrical resistivity imaging of cave Divaska Jama, Slovenia. J Cave Karst Stud 74(3):235–242

Anovitz LM, Cole R (2015) Characterization and analysis of porosity and pore structures. Rev Mineral Geochem 80(1):61–164. https://doi.org/10.2138/rmg.2015.80.04

Archie GE (1952) Classification of carbonate reservoir rocks and petrophysical considerations. AAPG Bull 36:278–298

Artugyan L, Ardelean AC, Urdea P (2015) Characterization of karst terrain usıng geophysical methods based on sinkhole analysis: A case study of the Anina Karstic Region (Banat Mountains, Romania). 14th Sinkhole Conference Nekri Symposium 5

Ayaz F (1995) Üst Kretase Yaşlı Şahinkaya Kireçtaşı'nın (Düzköy-Trabzon) mikrofasiyes incelemesi, MSc. Thesis, Karadeniz Teknik University, Graduate School of Natural and Applied Sciences, Trabzon, Turkey. Turkey Council of Higher Education, p.49 (in Turkish with English abstract)

Aydin F, Karsli O, Chen B (2008) Petrogenesis of the Neogene alkaline volcanics with implications for post-collisional lithospheric thinning of the Eastern Pontides, NE Turkey. Lithos 104(1–4):249–266

Babacan AE, Gelişli K, Tweeton D (2018) Refraction and amplitude attenuation tomography for bedrock characterization: Trabzon case (Turkey). Eng Geol 245:344–355

Balakrishna S, Balajı SM, Narshimulu G (2014) Ground Water potential in fractured aquifers of Ophiolite formations, Port Blair, South Andaman Islands using Electrical Resistivity Tomography (ERT) and Vertical Electrical Sounding (VES). J Geologıcal Socıety Indıa 83:393–402

Balkaya C, Göktürkler G, Erhan Z, Levent Ekinci Y (2012) Exploration for a cave by magnetic and electrical resistivity surveys: Ayvacık Sinkhole example, Bozdağ, İzmir (western Turkey). Geophysics 77(3):B135–B146

Barton NR, Lien R, Lunde J (1974) Engineering classification of rock masses for the design of tunnel support. Rock Mech 6(4):189–239

Batayneh AT, Abueladas AA, Moumani KA (2002) Use of ground-penetrating radar for assessment of potential sinkhole conditions: an example from Ghor Al Haditha area. Jordan Environ Geol 41:977–983. https://doi.org/10.1007/s00254-001-0477-8

Bear J (1972) Dynamics of fluids in porous media. Courier Corporation, New York

Bektaş O, Yılmaz C, Taslı K, Akdağ K, Özgür S (1995) Cretaceous rifting of the eastern Pontide carbonate platform, NE Turkey: the formation of carbonate breccias and turbidites as evidence of a drowned platform. Geologia 57:233–244

Bella P, Gaal L (2013) Genetic types of non-solution caves. In Proceedings of the 16th International Congress of Speleology (Vol. 3, pp. 237–242). Praha, Czech Republic: Speleological Society

Bermejo L, Ortega AI, Guerin R (2017) 2D and 3D ERT imaging for identifying karst morphologies in the archaeological sites of Gran Dolina and Galeria Complex (Sierra De Atapuerca, Burgos, Spain). Quatern Int 433:393–401

Bieniawski ZT (1989) Engineering rock mass classifications. Wiley, New York

Billi A, De Filippis L, Poncia PP, Sella P, Faccenna C (2016) Hidden sinkholes and karst cavities in the travertine plateau of a highly-populated geothermal seismic territory (Tivoli, central Italy). Geomorphology 255:63–80

Bulguroğlu N (1991) Düzköy-Çayırbağı yöresinin jeolojik incelemesi, MSc. Thesis, Karadeniz Teknik University, Graduate School of Natural and Applied Sciences, Trabzon, Turkey. Turkey Council of Higher Education, p.80 (in Turkish with English abstract)

Cardarelli E, Cercato M, Cerreto A, Di Filippo G (2010) Electrical resistivity and seismic refraction tomography to detect buried cavities. Geophys Prospect 58(4):685–695

Cardarelli E, Cercato M, De Donno G, Di Filippo G (2013) Detection and imaging of piping sinkholes by integrated geophysical methods. Near Surf Geophys 12(3):439–450

Carpenter PJ, Higuera-Diaz IC, Thompson MD, Atre M, Mandell W (2003) Accuracy of Seismic Refraction Tomography Codes at Karst Sites, 16th EEGS Symposium on the Application of Geophysics to Engineering and Environmental Problems, cp-190-00079

Ceru T, Segina E, Knez M, Benac C, Gosar A (2018) Detecting and characterizing unroofed caves by ground penetrating radar. Geomorphology 303:524–539

Chalikakis K, Plagnes V, Guerin R, Valois R, Bosch FP (2011) Contribution of geophysical methods to karst-system exploration: an overview. Hydrogeol J 19(6):1169

Cheng Q, Chen X, Tao M, Binley A (2019) Characterization of karst structures using quasi-3D electrical resistivity tomography. Environ Earth Sci 78:1–12

Chitea F, Stanciu IM, Ioane D (2019) Filled and unfilled underground voids evaluation using electrical resistivity method. In 19th International Multidisciplinary Scientific Geoconference SGEM 2019, Conference proceedings, Vol. 19, No. 1.1, pp. 795–802

Consorti L, Köroğlu F (2019) Maastrichtian-Paleocene larger Foraminifera biostratigraphy and facies of the Şahinkaya Member (NE Sakarya Zone, Turkey): insights into the Eastern pontides arc sedimentary cover. J Asian Earth Sci 183:1–15

Consorti L, Schlagintweit F, Köroğlu F, Rashidi K (2020) Stratigraphic record of Eponides Montfort, 1808 (benthic Foraminifera) from the Paleocene of the northern Neotethys margine. Micropaleontology 66(5):369–376

Cooper AH, Farrant AR, Price SJ (2011) The use of karst geomorphology for planning, hazard avoidance and development in Great Britain. Geomorphology 134(1–2):118–131

Cueto M, Olona J, Fernandez-Viejo G, Pando L, Lopez-Fernandez C (2018) Karst-induced sinkhole detection using an integrated geophysical survey: a case study along the Riyadh Metro Line 3 (Saudi Arabia). Near Surface Geophysics, 2018, 16, 270–281

Culver DC, White WB (2005) Encyclopedia of caves. Academic, p 661

Darcy H (1856) Les fontaines publiques de la ville de Dijon. Victor Dalmont, Paris

Davies WE, Morgan IM (1987) Geology of caves: US Geological Survey

Davis JL, Annan AP (1989) Ground-penetrating radar for high-resolution mapping of soil and rock stratigraphy. Geophys Prospect 37(5):531–551

De Groot-Hedlin C, Constable S (1990) Occam's inversion to generate smooth, two-dimensional models from magnetotelluric data. Geophysics 55:1613–1624. https://doi.org/10.1190/1.1442813

Deere DU, Miller RP (1966) Engineering classification and index properties for intact rock. Illinois Univ at Urbana Dept of Civil Engineering

Delle Rose M, Leucci G (2010) Towards an integrated approach for characterization of sinkhole hazards in urban environments: the unstable coastal site of Casalabate, Lecce, Italy. J Geophys Eng 7:143–154

Dhakate R, Amarender B, Kumar VS, Sankaran S, Rao VVSG (2015) Application of ground-penetrating radar for identification of groundwater resources in a coastal terrain. Arab J Geosci 8(7):4703–4715

Doğan U (2004) New approaches in doline classification. Gazi Eğitim Fakültesi Dergisi 24(1):249–269

Doolittle JA, Jenkinson B, Hopkins D, Ulmer M, Tuttle W (2006) Hydropedological investigations with ground-penetrating radar (GPR): estimating water-table depths and local ground-water flow pattern in areas of coarse-textured soils. Geoderma 131:3–4

Doyoro Y, Chang PY, Puntu JM (2021) Uncertainty of the 2D resistivity survey on the subsurface cavities. Appl Sci 11(7):3143

Drahor MG (2019) Identification of gypsum karstification using an electrical resistivity tomography technique: the case-study of the Sivas gypsum karst area (Turkey). Eng Geol 252:78–98

Dunham RJ (1962) Classification of Carbonate Rocks According to Depositional Textures in W.E. Ham. (Ed), Classification of Carbonate Rocks. AAPG Memoir 1, 108–121

Eker AM (2009) Ankara' nın kuzeyindeki pliyo-kuvaterner zeminlerin dinamik karakterlerinin ve yerel zemin koşullarının yüzey dalgası yöntemleri ile belirlenmesi, Msc. Thesis, Middle East Technical University, Graduate School of Natural and Applied Sciences, Ankara, Turkey. Turkey Council of Higher Education, p. 164 (in Turkish with English abstract)

El-Qady G, Hafez M, Ushıjıma K (2005) Imaging subsurface cavities using geoelectric tomography and ground-penetrating radar. J Cave Karst Stud v 67(3):174–181

Embry AF, Klovan JE (1971) A late devonian reef tract on northeastern Banks Island Nordwest Territories. Bull Can Pet Geol 19:730–781

Ersoy H, Kırmacı MZ, Ersoy AF (2006) Geology and formation of Yazkonağı Cave (Ünye-Ordu). J Geol Eng 30(1):39–48

Farfour M, Economou N, Abdalla O, Al-Taj M (2022) Integration of geophysical methods for doline hazard assessment: a Case Study from Northern Oman. Geosciences 12:243

Fatma K, Yacine D, Haydar B, Ahmed Y, Mohammed D, Karim H, Abdelatif B (2020) Use of electrical resistivity tomography (ERT) and electromagnetic induction (EMI) methods to characterize karst hazards in north-eastern of Algeria. Arab J Geosci 13:1204

Flügel E (2010) Microfacies of carbonate rocks: Analysis, interpretation and application, Springer, 2nd Edition. Springer, Berlin

Folk RL (1962) Spectral subdivision of limestone types. In: Ham, W.E. (Ed.), Classification of Carbonate Rocks. AAPG Memoir, 1, 62–84

Folk RL (1974) Petrology of sedimentary rocks. Hemphill Pub. Co., Austin

Ford D, Williams P (2007) Karst hydrogeology and geomorphology. John Wiley and Sons Ltd., England

Gan F, Han K, Lan F, Chen Y, Zhang W (2017) Multi-geophysical approaches to detect karst channels underground—A case study in Mengzi of Yunnan Province, China. J Appl Geophys 136:91–98

Gelişli K, Babacan AE (2021) Geophysical resistivity applications in groundwater exploration. J Eng Sci Des 9(2):535–543

Geometrics (2009) SeisImager/SWTM Manuel. OYO Corporation, USA

Gilbert P (1972) Iterative methods for the three-dimensional reconstruction of an object from projections. J Theor Biol 36:105–117

Gloaguen E, Chouteau M, Marcotte D, Chapuis R (2001) Estimation of hydraulic conductivity of an unconfined aquifer using cokriging of GPR and hydrostratigraphic data. J Appl Geophys 47(2):135–152

Gomez-Ortiz D, Pereira M, Martin-Crespo T, Rial FI, Novo A, Lorenzo H, Vidal JR (2009) Joint use of GPR and ERI to image the subsoil structure in a Sandy Coastal environment. E-Geo.Fcsh.Unl.Pt, no. 56, 2009, pp. 956–960

Goodman RE (1989) Introduction to Rock Mechanics. 2nd Edition, John Wiley & Sons Ltd., New York

Gosar A, Ceru T (2016) Search for an artificially buried karst cave entrance using ground penetrating radar: a successful case of locating the S-19 cave in the Mt. Kanin massif (NW Slovenia). Int J Speleol 45:135–147

Greenfield RJ (1979) Review of geophysical approaches to the detection of karst. Bull Assoc Eng Geol 16(3):393–408

Günan İ (2023) Trabzon İli Düzköy İlçesi Çalköy Mahallesi, 581 Ada, 1 Parsel ile 582 Ada, 1 Parsel içerisindeki 2.02 Ha alanın İmar Planına Esas Jeolojik & Jeoteknik Etüt Raporu. DO-ĞA Mühendislik Hiz. İnş. Mad. Ltd. Şti., ss. 107 (ekler), Trabzon/Türkiye. (in Turkish)

Halliburton (2001) Basic Petroleum Geology and Log Analysis. Halliburton

Hamilton WI (1842) Reseaches in Asia Minor. Pontus and Armenia II. London

Hasan MFR, Swastika TW, Martina N, Wulandari LS (2019) Identification of Groundwater distribution using self potential method. Appl Res Civil Eng Environ (ARCEE) 1(01):16–23

Hengari GM, Hall CR, Kozusko TJ, Bostater CR (2013) Use of ground penetrating radar for determination of water table depth and subsurface soil characteristics at Kennedy Space Center, Proc. SPIE 8893. Earth Resources and Environmental Remote Sensing/GIS Applications IV, 889318

Hiltunen DR, Cramer BJ (2008) Application of seismic refraction tomography in karst terrane. J Geotech GeoEnviron Eng, 134, Issue 7

Hippolyte JC, Müller C, Sangu E, Kaymakci N (2015) Stratigraphic comparisons along the Pontides (Turkey) based on new nannoplankton age determinations in the Eastern Pontides: geodynamic implications, vol 428. Geological Society London, pp 323–358

Honings JP (2022) Hydrogeologic investigation of a covered karst terrain, Louisiana State University at Baton Rouge, ''Doctor'' thesis, The Department of Geology and Geophysics, ABD

Hussain Y, Uagoda R, Borges W, Nunes J, Hamza O, Condori C, Aslam K, Dou J, Cardenas-Soto M (2020) The potential use of geophysical methods to identify cavities, sinkholes and pathways for water infiltration. Water 12:2289

Idi BY, Kamarudin MN (2011) Ground water estimation and water table detection with ground penetrating radar. Asian J Earth Sciencesv 4(3):193–202

Imposa S, Grassia S, Raimondob SD, Pattia G, Lombardoa G, Panzeraa F (2017) Seismic refraction tomography surveys as a method for voids detection: an application to the archaeological park of Cava Ispica, Sicily, Italy. Int J Architectural Herit 12(5):806–815

İnan N, İnan S, Kurt İ (1999) Doğu Pontidler'de Uyumlu Bentik K/T Geçişi: Tonya Formasyonu'nun (GB Trabzon) Şahinkaya Üyesi. Türkiye Jeoloji Bülteni 42(2):63–67

ISRM (1981) In: Brown ET (ed) Rock characterization, testing and monitoring, ISRM suggested methods. Pergamon

Jabrane O, Martinez-Pagan P, Martinez-Segura MA, Alcala FJ, El Azzab D, Vasconez-Maza MD, Charroud M (2023) Integration of Electrical Resistivity Tomography and Seismic Refraction Tomography to Investigate Subsiding sinkholes in Karst Areas. Water 15(12):2192

Jardani A, Revil A, Santos F, Fauchard C, Dupont JP (2007) Detection of preferential infiltration pathways in sinkholes using joint inversion of self-potential and EM-34 conductivity data. Geophys Prospect 55(5):749–760

Kaufmann O, Deceuster J (2014) Detection and mapping of ghost-rock features in the Tournaisis area through geophysical methods–an overview. Geologica Belgica

Kaufmann G, Romanov D (2009) Geophysical investigation of a sinkhole in the northern Harz foreland (North Germany). Environ Geol 58:401–405

Ketin İ (1966) Anadolu'nun tektonik birlikleri. MTA Dergisi 66:20–34 (in Turkish with English abstract)

Khaldaoui F, Djediat Y, Baker H, Ydri A, Djeddi M, Hamadou K, Bouzar A (2020) Use of electrical resistivity tomography (ERT) and electromagnetic induction (EMI) methods to characterize karst hazards in north-eastern of Algeria. Arab J Geosci 13:1204

Klimchouk A, Bayari S, Nazik L, Toerk K (2006) Glacial destruction of cave systems in high mountains, with a special reference to the Aladaglar massif, Central Taurus, Turkey. Acta Carsologica 35(2):111–121

Korkmaz S (1993) Stratigraphy of the Tonya-Düzköy (SW Trabzon) area, NE Turkey. Türkiye Jeoloji Bülteni 36:151–158

Köroğlu F (2018) Stratigraphical, micropaleontological and sedimentological investigation of Şahinkaya Member in Çayırbağı-Çalköy (Düzköy/Trabzon) region. MSc. Thesis, Recep Tayyip Erdogan University, Graduate School of Natural and Applied Sciences, Rize, Turkey. Turkey Council of Higher Education, Thesis No: 507559, p. 191 (in Turkish with English abstract)

Köroğlu F, Kandemir R (2019a) Vulnerable geosites of Çayırbağı-Çalköy (Düzköy/Trabzon) in the Eastern Black Sea region of NE Turkey and their geotourism potential. Geoheritage 11:1101–1111

Köroğlu F, Kandemir R (2019b) The biolithoclastic carbonate facies analysis: Şahinkaya Member Maastrichtian (late cretaceous) skeletal carbonate deposit, Sakarya Zone, NE Turkey. Carbonates Evaporites 34:1737–1755

Koster B, Kruse F (2016) The use of ground penetrating radar (GPR) in the investigation of historical quarry abandonment in Svalbard. Polar Record 52:330–344

Kowalczyk S, Lejzerowicz A, Kowalczyk B (2018) Groundwater table level changes based on ground penetrating radar images: a case study. 17th International Conference on Graund Penetrating Radar (GPR), 1–4

Kruse S, Grasmueck M, Weiss M, Viggiano D (2006) Sinkhole structure imaging in covered karst terrain. Geophys Res Lett, 33(16)

Kwon HS, Kım JH, Ahn HY, Kım KS, Jung CK, Lee SB, Uchıda T (2005) Delineation of a fault zone beneath a riverbed by an electrical resistivity survey using a floating streamer cable. Explor Geophys 36:50–58

Lago AL, Borges WR, Barros JS, de Sousa Amaral E (2022) GPR application for the characterization of sinkholes in Teresina, Brazil. Environ Earth Sci 81(4):132

Lange LA (1999) Geophysical studies at Kartchner Caverns State Park, Arizona. J Cave Karst Stud 61(2):68–72

Lavergne M (1986) Methodes sismiques. Edition Technip, Paris, France, 207 p

Lejzerowicz A, Wysocka A, Kowalczyk S (2018) Application of ground penetrating radar method combined with sedimentological analyses in studies of glaciogenic sediments in central Poland. Studia Quaternaria, 35

Leucci G (2006) Contribution of ground penetrating radar and electrical resistivity tomography to identify the cavity and fractures under the Main Church in Botrugno (Lecce, Italy). J Archaeol Sci 33(9):1194–1204

Loke MH (2010) Res2Dinv ver. 3.59 for Windows XP/Vista/7, 2010, Rapid 2-D Resistivity & IP Inversion Using the Least-Squares Method, Geoelectrical Imaging 2D & 3D Geotomo Software 2010, Malaysia

Lucia FJ (1995) Rock-fabric/petrophysical classification of carbonate pore space for reservoir characterization. https://doi.org/10.1306/7834d4a4-1721-11d7-8645000102c1865d. Bulletin

Lucia FJ (2004) Origin and petrophysics of dolostone pore space. Geol Soc Lond Spec Publ 235(1):141–155. https://doi.org/10.1144/GSL.SP.2004.235.01.06

Lucia FJ (2007) Carbonate reservoir characterization: an integrated approach. Springer, Berlin

Lucia FJ, Conti RD (1987) Rock fabric, permeability, and log relationships in an upward-shoaling, vuggy carbonate sequence: University of Texas at Austin, Bureau of Economic Geology. Geological Circular 87 – 5

Luo T, Xia J, Miller RD, Xu Y, Liu J, Liu O (2008) Rayleigh-Wave dispersive energy imaging using a high-resolution linear radon transform, Pure appl. geophys. 165 (2008) 903–922

Lyskowski M, Mazurek E, Zietek J (2014) Ground penetrating radar investigation of limestone karst at the Odstrzelona Cave in Kowala, Swietokrzyskie Mountains, Poland. J Cave Karst Stud, 76(3)

Mahmoudzadeh MR, Frances AP, Lubczynski M, Lambot S (2012) Using ground penetrating radar to investigate the water table depth in weathered granites-Sardon case study, Spain. J Appl Geophys 79:17–26

Martinez-Moreno FJ, Pedrera A, Ruano P, Galindo-Zaldivar J, Martos-Rosillo S, Gonzalez-Castillo L, Sanchez-Ubeda JP, Marin-Lechado C (2013) Combined microgravity, electrical resistivity tomography and induced polarization to detect deeply buried caves: Algaidilla cave (Southern Spain). Eng Geol 162:67–78

Martinez-Moreno FJ, Galindo-Zaldivar J, Pedrera A, Teixido T, Ruano P, Pena JA, Gonzalez-Castillo L, Ruiz-Constan A, Lopez-Chicano M, Martin-Rosales W (2014) Integrated geophysical methods for studying the karst system of Gruta De Las Maravillas (Aracena, Southwest Spain). J Appl Geophys 107:149–162

McCraw DJ, Land L (2016) Sinkholes: a hidden, real New Mexico Geohazard. New Mexico Earth Matter 16(1):1–6

McGrath RC, Styles P, Thomas ES, Neale S (2002) Integrated high-resolution geophysical investigations as potential tools for water resource investigations in karst terrain. Environ Geol 42:552–557

McMechan GA, Loucks RG, Mescher P, Zeng X (2002) Characterization of a coalesced, collapsed paleocave reservoir analog using GPR and well-core data. Geophysics 67(4):1148–1158

Mylroie JE (2019) Coastal caves. Encyclopedia of caves. Academic, pp 301–307

Nakashima Y, Zhou H, Sato M (2001) Estimation of groundwater level by GPR in an area with multiple ambiguous reflections. J Appl Geophys 47(3–4):241–249

Nasri F, Boumezbeur A, Benavente D (2019) Influence of the petrophysical and durability properties of carbonate rocks on the deterioration of historic constructions in Tebessa (northeastern Algeria). Bull Eng Geol Environ 78:3969–3981. https://doi.org/10.1007/s10064-018-1410-7

Nazik L, Bayarı S (2018) Mavi Gezegen. Mağara zengini ülke: Türkiye, 24:7–19

Nazik L, Poyraz M (2015) Role of neotectonics in karst morphology of Turkey, IV. Ulusal Jeomorfoloji Sempozyumu Bildiriler Kitabı, s.203–213, Samsun

Nazik L, Poyraz M (2017) A region that characterise the general karst geomorphology of Turkey: Central Anatolia Plateau karst zone. Türk Coğrafya Dergisi 68:43–56

Nikishin AM, Okay A, Tüysüz O, Demirer A, Amelin N, Petrov E (2015a) The Black Sea basins structure and history: new model based on new deep penetration regional seismic data. Part 1: basin structure and fill. Mar Pet Geol 59:638–655

Nikishin AM, Okay A, Tüysüz O, Demirer A, Wannier M, Amelin N, Petrov E (2015b) The Black Sea basins structure and history: new model based on new deep penetration regional seismic data. Part 2: tectonic history and paleogeography. Mar Pet Geol 59:656–670

Nwokebuihe S, Torgashov E, Anderson N (2014) A description of an effective sinkhole investigation approach: a case study of a site in Greene County, Missouri. In Symposium on the Application of Geophysics to Engineering and Environmental Problems 2014 (pp. 304–318). Society of Exploration Geophysicists and Environment and Engineering Geophysical Society

Nyquist JE, Freyer PA, Toran L (2008) Stream bottom resistivity tomography to map ground water discharge. Ground Water 46:561–569

Oberender P, Plan L (2013) A genetic classification of caves in Lower Austria. In Proceedings 16th international congress of speleology, Czech Republic, Brno (Vol. 3, pp. 390–392)

Oberender P, Plan L (2018) A genetic classification of caves and its application in eastern Austria. Geol Soc Lond Special Publications 4661:121–136

Obi JC (2016) Geophysical imaging of karst features in Missouri. Missouri University of Science and Technology

Odum JK (2007) Near surface shear wave velocity versus depth profiles, Vs30, and NEHRP classifications for 27 sites in Puerto Rico. USGS. U.S. Geological Survey

Ofluoğlu S (1993) Çalköy-Alazlı (Düzköy-Trabzon) Yöresinin Karstlaşma Yönünden İncelenmesi. MSc. Thesis, Karadeniz Technical University, Graduate School of Natural and Applied Sciences, Trabzon, Turkey. Turkey Council of Higher Education, p. 65 (in Turkish with English abstract)

Okay AI, Şahintürk Ö (1997) Geology of the Eastern Pontides. In: Robinson A (ed) Regional and petroleum geology of the Black Sea and surrounding regions: American Association of Petroleum Geologists (AAPG) 68, USA, pp 291–311

Orojah OJ, Agayina KE (2014) Hydro-geophysical investigation using seismic refraction tomography to study the groundwater potential of Ahmadu Bello University Main Campus, within the basement complex of Northern Nigeria. J Environ Earth Sci. 4, 2

Osswald F (1912) Armenian-Handbuch der Regionalien Geologie, 10, 3, Heidelberg

Özer S, Meriç E, Görmüş M, Kanbur S (2009) Biogeographic distribution of rudists and benthic foraminifera: an approach to Campanian– Maastrichtian palaeobiogeography of Turkey. Geobios 42:623–638

Özsayar T, Pelin S, Gedikoğlu A (1981) Doğu Pontidler'de Kretase. Karadeniz Teknik Üniversitesi Yer Bilimleri Dergisi Jeoloji 1/2:65–114

Öztürk MZ (2018) Karstik kapalı depresyonların (dolinlerin) morfometrik analizleri. Coğrafya Dergisi, (36), 1–13

Palmström A (1996) Characterizing rock masses by the RMi for use in practical rock engineering: part 1: the development of the Rock Mass index (RMi). Tunn Undergr Space Technol 11(2):175–188

Pandey AK, Gogoi J, Pandey P (2019) Mapping shallow subsurface to identify sinkhole formation in urban areas using ground penetration radar: a Case Study from Hyderabad, India. Curr Sci 117(10):25

Park CB, Miller RD, Xia J (1998) Imaging dispersion curves of surface waves on multi-channel record. In: SEG technical program expanded abstracts, New Orleans, LA; 1998, pp. 1377–80

Park MK, Park S, Yi MJ, Kim C, Son JS, Kim JH, Abraham AA (2014) Application of electrical resistivity tomography (ERT) technique to detect underground cavities in a karst area of South Korea. Environ Earth Sci 71:2797–2806

Parker EH, Hawman R (2011) Multi-channel analysis of surface waves (MASW) in karst terrain, Southwest Georgia: implications for detecting anomalous features and fracture zones. J Environ Eng Geophys 17(3):129–150

Pentecost A (2005) Travertine. Springer, Berlin-Heidelberg

Prins C, Thuro K, Krautblatter M, Schulz R (2019) Testing the effectiveness of an inverse Wenner-Schlumberger array for geoelectrical karst void reconnaissance, on the swabian Alb high plain, new line Wendlingen–Ulm, southwestern Germany. Eng Geol 249:71–76

Putiska R, Kusnırak D, Dostal I, Lacny A, Mojzess A, Hok J, Pasteka R, Krajna M, Bosansky M (2014) Integrated geophysical and geologıcal investigations of karst structures in Komberek, Slovakia. J Cave Karst Stud, 76(3)

Revil A, Jardani A (2013) The self-potantial method: theory and applications in environmental geosciences. Cambridge University Press, p 319

Robert T, Dassargues A, Brouyere S, Kaufmann O, Hallet V, Nguyen F (2011) Assessing the contribution of electrical resistivity tomography (ERT) and self-potential (SP) methods for water well drilling program in fractured/karstified limestones. J Appl Geophys 75(1):42–53

Robinson AG, Banks CJ, Rutherford MM, Hirst JPP (1995) Stratigraphic and structural development of the Eastern Pontides, Turkey. J Geol Soc 152(5):861–872

Robinson M, Bristow C, McKinley J, Ruffell A (2013) Ground penetrating radar school of geography, archaeology and palaeoecology, Queen's University Belfast 2. Department of Earth and Planetary Sciences, Birkbeck University of London

Rodriguez V, Gutierrez F, Green AG, Carbonel D, Horstmeyer H, Schmelzbach C (2014) Characterizing sagging and collapse sinkholes in a mantled karst by means of ground penetrating radar (GPR). Environ Eng Geosci 20:109–132

Sandmeier KJ (2015) ReflexW version 7.5 - program for the processing of seismic, acoustic or electromagnetic reflection, refraction and transmission data, p. 604

Sarıbudak M (2015) The Million Dollar Question: Which geophysical methods locate caves best over the Edwards Aquifer? A Potpourri of Case Studies from San Antonio and Austin, Texas, USA, Sinkholes and the Engineering and Environmental Impacts of Karst: Proceedings of the Fourteenth Multidisciplinary Conference

Sarıbudak M, Hauwert NM (2017) Integrated geophysical investigations of Main Barton Springs, Austin, Texas, USA. J Appl Geophys 138:114–126

Sarıbudak M, Hawkins A (2019) Hydrogeopysical characterization of the Haby crossing fault, San Antonio, Texas, USA. J Appl Geophys 162:164–173

Sayed SRM, Elkhedr HI, Eslam E, Mohamed M, Naser A (2012) Seismic refraction and resistivity imaging for assessment of groundwater seepage under a dam site, Southwest of Saudi Arabia. Int J Phys Sci 7(48):6230–6239

Schlumberger Oilfield Glossary (2023) Schlumberger Oilfield Glossary. Porosity unit - Schlumberger Oilfield Glossary. https://www.glossary.oilfield.slb.com/Terms/p/porosity_unit.aspx. Accessed 23 June 2023

Şeren A, Babacan AE, Gelişli K, Ögretmen Z, Kandemir R (2012) An investigation for potential extensions of the Karaca Cavern using geophysical methods. Carbonates Evaporites 27:321–329

Sevil J, Gutierrez F, Zarroca M, Desir G, Carbonel D, Guerrero J, Linares R, Roque C, Fabregat I (2017) Sinkhole investigation in an urban area by trenching in combination with GPR, ERT and high-precision leveling. Mantled evaporite karst of Zaragoza city, NE Spain. Eng Geol 231:9–20

Singh KKK, Bharti AK, Pal SK, Prakash A, Saurabh Kumar R, Singh PK (2019) Delineation of fracture zone for groundwater using combined inversion technique. Environ Earth Sci 78:1–12

Stevanovic Z, Dragisic V (1998) An example of identifying karst groundwater flow. Environ Geol 35:241–244

Su LJ, Xu XQ, Geng XY, Liang SQ (2017) An integrated geophysical approach for investigating hydro-geological characteristics of a debris landslide in the Wenchuan earthquake area. Eng Geol 219:52–63

Tao M, Chen X, Cheng Q, Binley A (2022) Evaluating the joint use of GPR and ERT on mapping shallow subsurface features of karst critical zone in southwest China. Vadose Zone J, 21(1), e20172

Telford WM, Geldart LP, Sheriff RE (1991) Applied geophysics, 2nd edn. Cambridge University Press, page, New York, p 770

Törk K, Çakır K, Kahraman İ (2013) Çal Mağarası (Trabzon-Düzköy) Araştırma Raporu

Tucker ME, Wright VP (1990) Carbonate sedimentology. Blackwell, Oxford

Türk-Öz E, Özyurt M (2018) Palaeoenvironment reconstruction and planktonic foraminiferal assemblages of Campanian (cretaceous) carbonate succession, Çayırbağ area (Trabzon, NE Turkey. Carbonates Evaporites 33:1–33

Ugwu S, Nwankwoala HO (2008) Application of seismic refraction methods in groundwater studies in Calabar Southeastern Nigeria", Scientia Africana, Vol. 7 No. 2

Uzun A, Zeybek HI, Yılmaz C, Bahadır M (2015) Aksu Çayı havzası Traverten Mağaraları, Giresun. Marmara Coğrafya Dergisi 31:243–257

Valois R, Bermejo L, Guerin R, Hinguant S, Pigeaud R, Rodet J (2010) Karstic morphologies identified with geophysics around Saulges caves (Mayenne, France). Archaeol Prospection 17(3):151–160

Valois R, Camerlynck C, Dhemaied A, Guerin R, Hovhannissian G, Plagnes V, Rejiba F, Robain H (2011) Assessment of doline geometry using geophysics on the Quercy plateau karst (South France). Earth Surf Proc Land 36(9):1183–1192

Venkatanarayana B, Rao TV (1989) Geological and geophysical investigations for delineating karstic structures of the southwestern portion of Cuddapah basin, Andhra Pradesh, India. In: Berry BF (ed) Proceedings of 3rd multidisciplinary conference on sinkholes and the engineering and environmental impacts of Karst, USA, Balkema, Dordrecht, The Netherlands, pp 59–64

Verdet C, Sirieix C, Marache A, Riss J, Portais JC (2020) Detection of undercover karst features by geophysics (ERT) Lascaux cave hill. Geomorphology 360:107177

Veress M (2016) Covered karsts. Institute of Geography and Environmental Sciences. Szombathely, Hungary

Vichabian Y, Morgan FD (2002) Self potentials in cave detection. Lead Edge 21(9):866–871

Voytek EB, Barnard HR, Jougnot D, Singha K (2019) Transpiration- and precipitation-induced subsurface water flow observed using the self-potential method. Hydrol Process 33(13):1784–1801

Waltham AC, Fookes PG (2005) Engineering classification of karst ground conditions. Q J Eng GeolHydrogeol 36(2):101–118

Wanfang Z, Beck BF, Stephenson JB (1999) Investigation of groundwater flow in karst areas using component separation of natural potential measurements. Environ Geol 37(1–2):19–25

Williams MA, Ziegler S (2014) Local regulatory protection for ecosystem services: A Case study from the Karst Region of Southeast Minnesota, USA

Xu XQ, Su LJ, Lıang SQ (2015) A review of geophysical detection methods of landslide structure characteristics. Progress İn Geophys 30(3):1449–1458

Yılmaz Ö (1987) Seismic data processing. Society of Exploration Geophysicists, Tulsa, OK

Yılmaz Y, Tüysüz O, Yiğitbas E, Can Genç Ş, Şengör AMC (1997) Geology and tectonic evolution of the pontides. In: Robinson

Young ME, De Bruijn RGM, Al-Ismaily AS (1998) Exploration of an alluvial aquifer in Oman by time-domain electromagnetic sounding. Hydrogeol J 6:383–393

Yücel C, Arslan M, Temizel İ, Abdioğlu E (2014) Volcanic facies and mineral chemistry of tertiary volcanics in the northern part of the Eastern Pontides, northeast Turkey: implications for pre-eruptive crystallization conditions and magma chamber processes. Mineral Petrol 108:439–467

Zaman M, Şahin İF, Birinci S (2011) Çal Mağarası Düzköy Trabzon ve çevresinin ekoturizm potansiyeli açısından önemi. East Geo Rev 26:1–23 (in Turkish)

Zeybek İ (2010) Canik Dağlarının güneydoğu bölümünde karstlaşma ve karstik şekiller. Doğu Coğrafya Dergisi 24:93–115

Zhou W, Beck BF, Stephenson JB (2000) Reliability of dipole-dipole electrical resistivity tomography for defining depth to bedrock in covered karst terranes. Environ Geol 39:7

Publisher's Note Springer Nature remains neutral with regard to jurisdictional claims in published maps and institutional affiliations.